Journal of Iberian Geology
https://doi.org/10.1007/s41513-024-00271-9

RESEARCH PAPER

Iron-carbonate concretions with inverse magnetic fabrics; a record of environmental changes in the middle Eocene marine marls of the Southern Pyrenees?

B. Oliva-Urcia[1] · J. C. Larrasoaña[2,3] · A. Travé[4] · M. Garcés[5] · P. Sierra-Campos[3] · E. L. Pueyo[3] · P. Calvín[3]

Received: 8 April 2024 / Accepted: 23 October 2024

Abstract

This paper deals with the detailed analyses of magnetic fabrics, accompanied by stable isotopic composition and microscopic observations, in centimetric and metric scale authigenic carbonate concretions embedded in the Eocene flysch deposits of the Southwestern Pyrenees. Sampling was focused in the carbonate concretions, (in both metric and centimetric scale), in the marls lateral and nearby to the concretions and in the marls located several meters away from the concretions. The inverse magnetic fabrics (k_{max} axes cluster perpendicular to bedding plane) detected in these concretions constitute a fast methodology to uncover the presence of iron-carbonate minerals and the paleoenvironmental significance of their authigenic origin. The subfabric analyses indicate that magnetite is present in all four types of samples with normal magnetic fabric (k_{min} axes perpendicular to bedding). Paramagnetic fabric (low temperature anisotropy of magnetic susceptibility when magnetic susceptibility increases ~ 3.8 times the one at room temperature) overlaps the room temperature magnetic fabric. The microscope observations reveal that iron-enriched dolomite is the main carrier of the inverse fabric in the carbonate concretions at room temperature. The stable isotopic composition indicates minor differences between the Eocene marls and the carbonate concretions and, when compared with previous data, they suggest a marine pore water origin due to bacterial activity during burial. We relate the early diagenetic growth of the concretions to an enhancement in bacterial activity driven by the increased terrigenous and terrestrial organic matter supply during the Middle Eocene Climate Optimum (MECO), a period of global warming.

Keywords Inverse magnetic fabrics · Carbonate concretions · Fluid migration · Carbon sink

✉ B. Oliva-Urcia
boliva@unizar.es

J. C. Larrasoaña
jc.larra@igme.es

A. Travé
atrave@ub.edu

M. Garcés
mgarces@ub.edu

P. Sierra-Campos
p.sierra@igme.es

E. L. Pueyo
unaim@igme.es

P. Calvín
p.calvin@igme.es

[1] Geotransfer-IUCA, Departamento de Ciencias de la Tierra, Universidad de Zaragoza, 50009 Zaragoza, Spain

[2] Departamento de Ciencias, Universidad Pública de Navarra, 31006 Pamplona, Spain

[3] Instituto Geológico y Minero de España (IGME-CSIC), Campus Aula Dei. Av. Montañana 1005, 50059 Saragossa, Spain

[4] Sedimentary Geology. Departament de Mineralogia, Petrologia i Geologia Aplicada, Institut Geomodels. Facultat de Ciències de la Terra, Universitat de Barcelona (UB), 08028 Barcelona, Spain

[5] Grup de Geodinàmica I Anàlisi de Conques (GGAC), Universitat de Barcelona, Barcelona, Spain

Published online: 09 December 2024

Inverse fabrics in Eocene carbonate concretions of the Pyrenees, a sign of warmer paleoenvironment

Resumen

Este artículo trata el análisis detallado de la fábrica magnética junto con la composición de isótopos estables y observaciones microcópicas, realizado en concreciones carbonatadas autigénicas de tamaño métrico y centimétrico que se encuentran embebidas en depósitos de tipo flysch del Eoceno en la zona Surpirenaica. El muestreo se centró en las concreciones carbonatadas (en las de tamaño métrico y centimétrico), en las margas próximas y localizadas lateralmente a las concreciones y en las margas alejadas varios metros de las concreciones. La fábrica magnética inversa (los ejes k_{max} se agrupan perpendiculares al plano de estratificación) detectada en las concreciones constituye un método rápido para descubrir la presencia de minerales carbonatados con hierro y el significado paleoambiental de su origen autigénico. Los análisis de subfábricas indican que la magnetita está presente en los cuatro tipos de muestras con fábrica normal (los ejes k_{min} se localizan perpendiculares al plano de estratificación). La fábrica paramagnética (la anisotropía magnética medida a baja temperatura, cuando la susceptibilidad magnética aumenta ~3.8 veces la susceptibilidad magnética a temperatura ambiente) se superpone a la fábrica magnética medida a temperatura ambiente. Las observaciones al microscopio revelan que la dolomita enriquecida en hierro es el principal portador de la fábrica inversa a temperatura ambiente en las concreciones carbonatadas. La composición de isótopos estables indica diferencias menores entre las margas del Eoceno y las concreciones carbonatadas y, cuando se comparan con datos previos, sugieren un origen marino debido a actividad bacteriana durante el enterramiento. Relacionamos el crecimiento diagenético temprano de las concreciones debido a un aumento en la actividad bacteriana que a su vez es debida al aumento de terrígenos y materia orgánica terrestre que se da durante el Óptimo Climático del Eoceno Medio (MECO, por sus siglas en inglés), un periodo de calentamiento global.

Palabras clave Fábrica magnética inversa · Concreciones carbonatadas · Migración de fluidos · Sumidero de carbono

1 Introduction

The term "concretion" refers to local concentrations of authigenic mineral species that show contrast with the surrounding host rocks. Concentric growth occurs where successive layers of cement are added from the concretion center to the outer margin (Selles-Martínez, 1996; Wanas, 2008). The early-formed carbonate concretions may preserve the original phyllosilicate fabric as well as develop pressure shadows adjacent to concretions that would also suggest early concretion formation (Day-Stirrat et al., 2008 and references therein).

The precipitation of authigenic carbonate embedded in marine siliciclastic lithological series is usually related to a wide array of causes (i.e., methane migration, hydrocarbon seepage, hydrothermal fluids migration), but the most common causes are the ones related to syndepositional processes during burial diagenesis due to microbial degradation of organic matter and the associated changes in pore water chemistry (Coleman, 1993; Reinhold, 1998; Stakes et al., 1999; Wanas, 2008). Thus, microbial activity is linked to the use of oxidants to degrade buried organic matter, which follows a sequence that goes from more efficient to less efficient oxidant chemical species until organic matter is eventually exhausted (Froelich et al., 1979; Roberts, 2015). These species are oxygen (which is consumed during oxic conditions), nitrate, manganese and iron oxides (consumed during suboxic conditions), and sulphate and carbon dioxide (consumed under anoxic conditions). Microbially-mediated reduction of sulphate during earliest diagenesis releases sulphide, which reacts with iron-bearing minerals and dissolved iron to form pyrite and other iron sulphides. When the content of organic matter is higher, sulphate is eventually exhausted so that reduction of carbon dioxide takes place and results in the formation of methane (Froelich et al., 1979; Roberts & Weaver, 2005). Under these conditions, dissolved iron can react with other ions to form other authigenic minerals, including iron-bearing carbonates if pore waters become saturated with respect to bicarbonate (Raiswell & Fisher, 2004). For that to occur the alkalinity needs to increase, since methanogenesis produces methane and CO_2 that consequently lowers pH, which in turn dissolves carbonates. It is possible to enhance alkalinity with siliciclastic weathering in anoxic sediments along continental margins, since methanogenesis induces weathering of silica phases and promotes carbonate formation (Torres et al., 2020 and references therein). The formation of authigenic carbonates, which include dolomite, siderite and Fe-rich calcite, implies a sequestration of carbon from Earth's surface (Torres et al., 2020).

The isotopic composition of the carbonate concretion and mineralogical variability have been used to assess the composition of the source fluids, diagenetic processes in marine synsedimentary-diagenetic environments, or marine circulation (Aloisi et al., 2000). Therefore, large $\delta^{13}C$ depletions of authigenic calcite, aragonite and dolomite

may indicate methane as a major carbon source for the carbonate, for example around mud volcanoes in the sea floor where hydrocarbon gas seepage known as cold seeps occurs (Aloisi et al., 2000). Therefore, depletions of $\delta^{13}C$ are not necessarily related to variations of temperature. When variations in the ^{18}O are concomitant with variations in $\delta^{13}C$, then carbonate concretions can be interpreted as due to precipitation from ^{18}O-rich fluids and not due to a change in temperature effect (Aloisi et al., 2000). However, depletions of $\delta^{13}C$ in foraminifera of siliciclastic sediments in marine environments and in pedogenetic concretions indicate warm periods, such as the Paleocene-Eocene thermal maximum (PETM) (Rosales pers, comm.; Schmitz et al., 2001; Schmitz & Pujalte, 2003; Pujalte et al., 2009). In this case, the addition of light carbon in large quantities into the Earth system is claimed to be the main cause for the greenhouse effect. Therefore, a way to detect warmer periods with similar origin is to look for excursions in $\delta^{13}C$.

Ferroan carbonates (carbonates with Fe in their crystalline structure) such as siderite (iron carbonate) or ankerite (calcium and iron carbonate) have a characteristic inverse magnetic fabric at room temperature. One of the first definitions of inverse magnetic fabric at room temperature indicates that there is an interchange between the maximum (k_{max}) and minimum (k_{min}) axes of the magnetic fabric ellipsoid. They have been reported in single domain (SD) magnetite and ferroan carbonates among other minerals (Rochette, 1988). SD magnetite will provide a normal fabric when analyzing the anisotropy of the remanence -AARM- (Rochette, 1988; Imhlé et al., 1989 and references therein). Magnetic fabrics are used to obtain the orientation distribution of grains in a volume of rock in a fast and non-destructive way (Tarling and Hrouda, 1993; Borradaile & Jackson, 2010), and such inverse magnetic fabrics usually are described when the maximum axis is perpendicular to the bedding plane (or another structural surface such as the foliation plane), which is not "normal". One inverse magnetic fabric classification has been recently proposed after considering not only the orientation of the magnetic fabric ellipsoid but also the orientation of the c-axis of the crystal (the magnetocrystalline anisotropy, typical for each mineral). Therefore, there can be three types of inverse magnetic fabric, (i) pure inverse as in tourmaline or goethite (k_{max} axis perpendicular and c-axis parallel to the reference surface), (ii) simple inverse as in ankerite and siderite (k_{max} axis and c-axis perpendicular to the reference surface), and (iii) pseudo-normal as in calcite, (k_{max} axis parallel and c-axis perpendicular to the reference surface), (see Fig. 7 in Cerny et al., 2020). In normal fabric, the k_{max} axes and the crystallographic axes are on the considered surface (either bedding or tectonic foliation planes) (Cerny et al., 2020). This classification leaves out intermediate magnetic fabrics, that are presented in prior models, i.e., considering the inclination of the three magnetic ellipsoid axes after bedding correction, a triangular diagram can be constructed, as in Chadima et al. (2006), reviewing Rochette et al. (1992); Imhlé et al. (1989) and Ferré (2002). Hounslow (2001) described magnetic fabrics in siderite concretions concluding that the nucleation substrate ultimately dictates the crystallographic orientation of the carbonates in the concretion, finding the crystallographic c-axis near the bedding plane (in non-marine siderite) and perpendicular to the bedding plane (in marine siderite). He even considered different bands of siderite with different crystal orientations, and hence of the magnetic anisotropy. In later works, the models described by Hunslow (2001) are used to deduce the flow direction in pelitic rocks with the magnetic fabric carried by siderite (de Wall & Warr, 2004).

In this paper we present the magnetic fabrics (room temperature AMS) and subfabrics (low temperature AMS and anisotropy of the anhysteretic remanent magnetization -AARM) of the carbonate concretions and their surrounding marls in order to unravel the distinct petrofabric of the carbonate concretions. The sampled rocks are from the Middle Eocene Southpyrenean basin. Combining magnetic information and optical and compositional observations (electron scanning microscopy, cathodoluminescence) helps to constrain the characteristics of the carbonate concretions in order to examine their sedimentary significance in the paleogeographic and paleoclimatic evolution of the basin during the middle Eocene time. The distinct petrofabric between the carbonate concretions and the surrounding rocks can be used as a fast and non-destructive way to characterize authigenic ferroan-carbonate concretions.

2 Geological location

The carbonate concretions and marls were sampled in one locality at the northern limb of the Izaga syncline. The Izaga syncline is an alpine structure situated in the Jaca-Pamplona basin, South Pyrenean Zone (Fig. 1). The Jaca-Pamplona basin developed during the alpine compression (Late Cretaceous-Miocene) from an Eocene foreland type basin (flysch deposits) in its early evolution to a piggy-back type basin in its latest stages until is infill with the Oligo-Miocene molasse deposits (Puigdefàbregas, 1975). The deposition of the deepest sediments in the basin (Eocene flysch) is contemporaneous with the emplacement of an imbricated system of thrusts and associated folds (Larra-Monte-Perdido thrust system) during the Eocene in the northern part of the basin (Labaume et al., 1985; Teixell, 1998). The structures have a WNW-ESE orientation and are mostly directed towards the South. The basin was susbsequently affected by other basement thrusts (Gavarnie and Guarga) developed according to a piggy-back sequence, in such a way that was involved in the Pyrenean deformation till it was eventually exhumed and eroded during

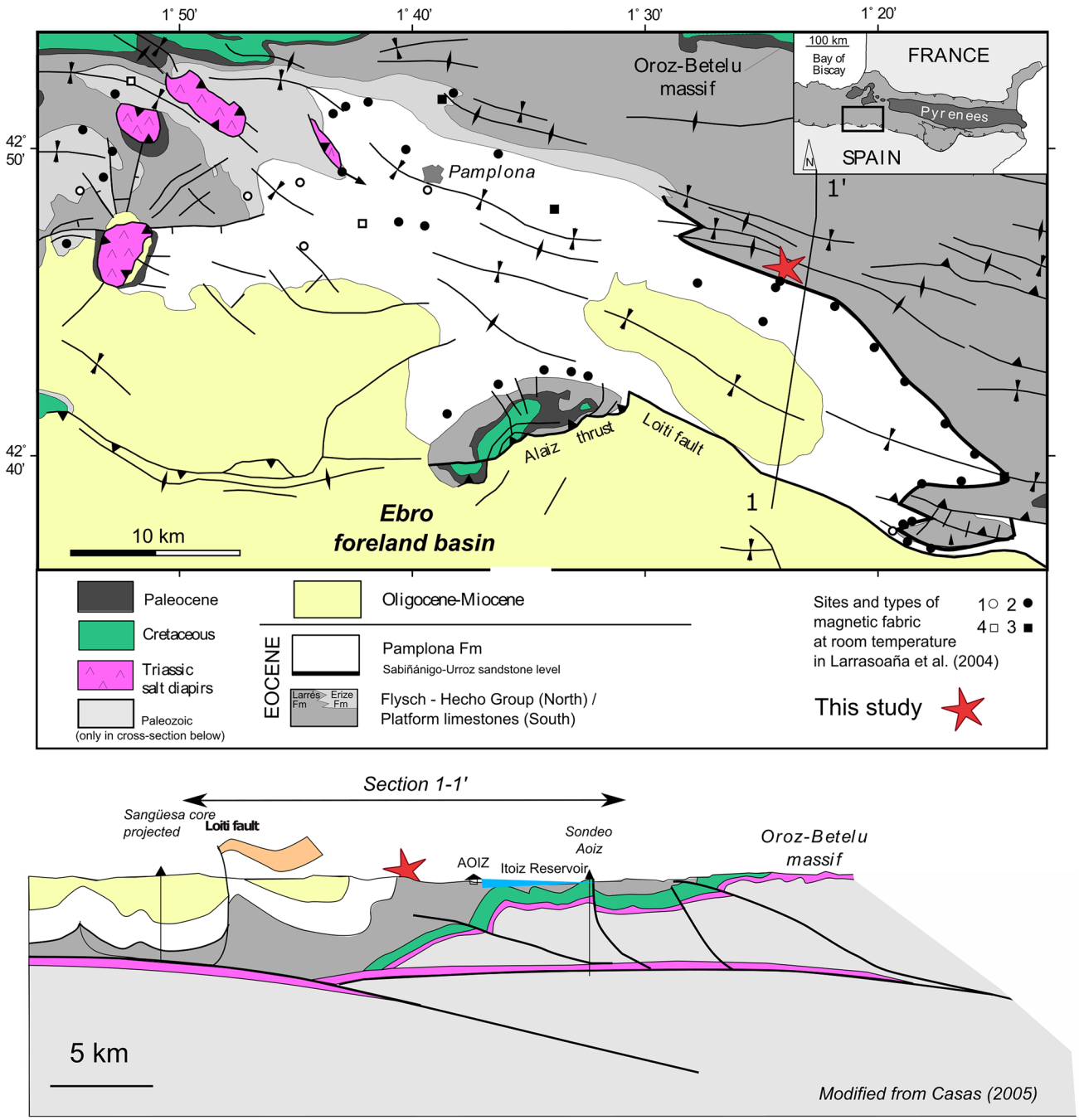

Fig. 1 The geological map for the study area and cross-sections with the interpretation for the general structure (from Casas, 2005). Types of magnetic fabric from Larrasoaña et al. (2004) are: (1) undeformed, (2) initial alignment of k_{max} axes perpendicular to the shortening direction, (3) k_{max} axes cluster parallel to fold axis and k_{min} and k_{int} axes form a pseudo-girdle, (4) similar as in 3, but k_{min} and k_{int} axes form a clear girdle distribution

Oligocene to Miocene times (Teixell, 1996, 1998). Although the detailed geometry of the structure in the study area varies among different authors, all the interpretations agree in the presence of south directed thrusts and associated folds (Casas, 2005; Oliva-Urcia et al., 2012; Ruiz et al., 2006). The study area is located at the northern limb of the Izaga syncline, which displays a subvertical attitude and enables the exposure of the sediments that record the tectonic evolution of the Jaca-Pamplona basin (Mutti et al., 1999; Puigdefàbregas, 1975; Remacha et al., 2005) (Fig. 2): (i) the uppermost part of the Hecho Group, a sequence of up to 4500 m of lower Eocene (Ypresian to Lutetian) hemipelagic marls and

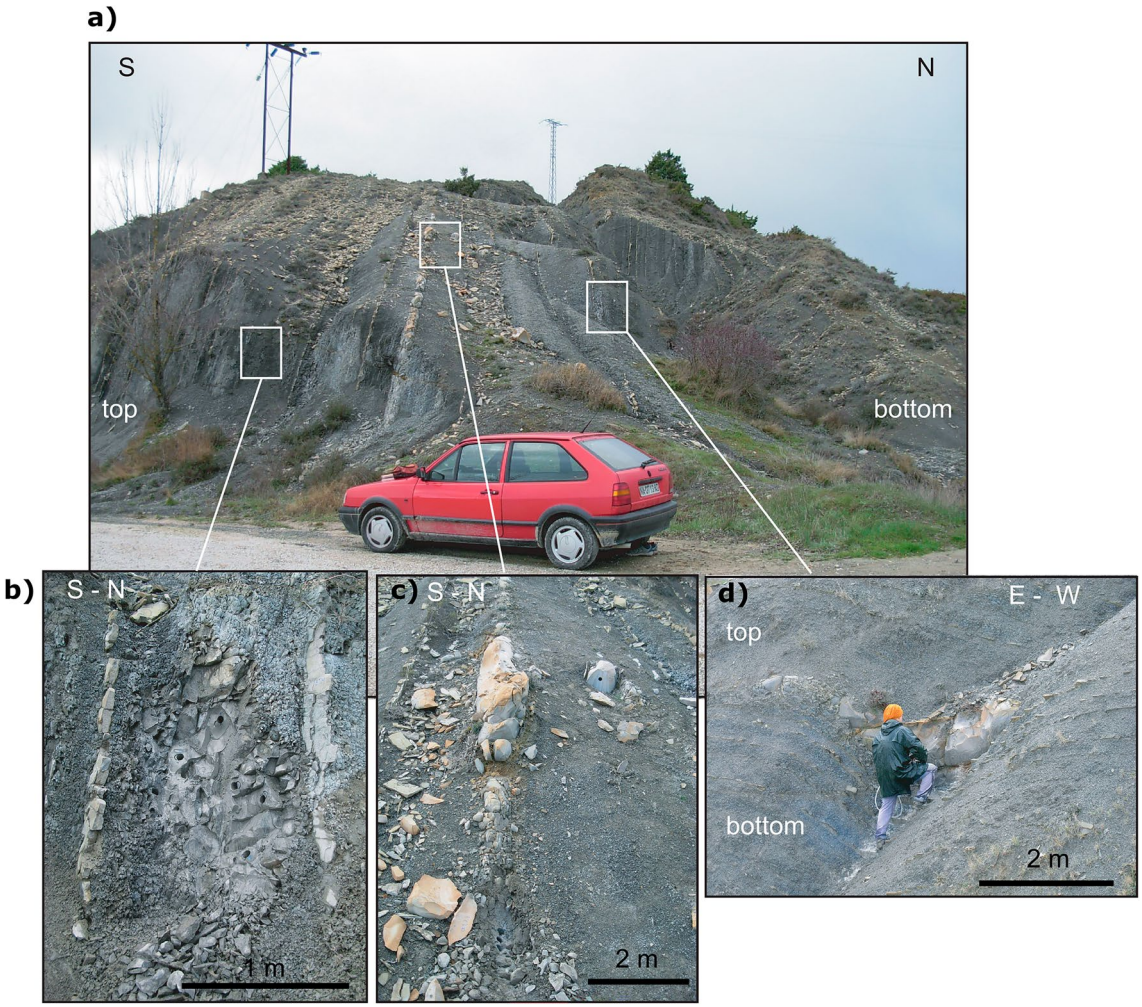

Fig. 2 Field pictures of the sampled carbonate concretions and marls. **a** General picture, **b** Distant marls, **c** centimetric carbonate concretion and near marls, **d** metric carbonate concretion

turbiditic sandstones that attest to deep-water sedimentation when the basin constituted an E-W oriented foredeep developed in response to tectonic load in the northern part of the mountain belt; (ii) the Larrés Formation, an up to 500 m-thick succession of middle Eocene (Lutetian to Bartonian) marls with subsidiary thin turbidites that signal the transition from deep-water turbiditic to slope prodeltaic sedimentation; (iii) the Urroz Formation, a 100-m thick succession of Bartonian siltstones that mark the sudden westward progradation of deltaic systems sourced from the emerged areas of the Central Pyrenees; and (iv) the lower part of the Pamplona Formation, a 2000 m-thick sequence of middle-upper Eocene (Bartonian to Priabonian) prodeltaic marls that attest to the later infill of the basin that culminated with its continentalization during the late Bartonian.

The studied carbonate concretions appear embedded within the marls that constitute the uppermost part of the Larrés Formation, about 50–250 m below the base of the Urroz Formation and its lateral counterpart to the east, the deltaic sandstones of the Sabiñánigo Formation (Remacha et al., 2005). Noticeably, carbonate concretions like the ones studied here have been reported from other sectors of the Jaca-Pamplona basin (Boya, 2019), although at a somehow lower position within the Larrés Formation.

3 Methodology

The methodology applied in this work includes: (i) the sampling of 40 specimens oriented in the field, (ii) the analyses of the magnetic fabric and magnetic properties (room and low temperature AMS, anisotropy of the anhysteretic remanent magnetization –AARM–), partial anhysteretic remanent magnetization and thermal demagnetization of three components isothermal remanent magnetization. (iii) the analyses of the compositional and textural characteristics of

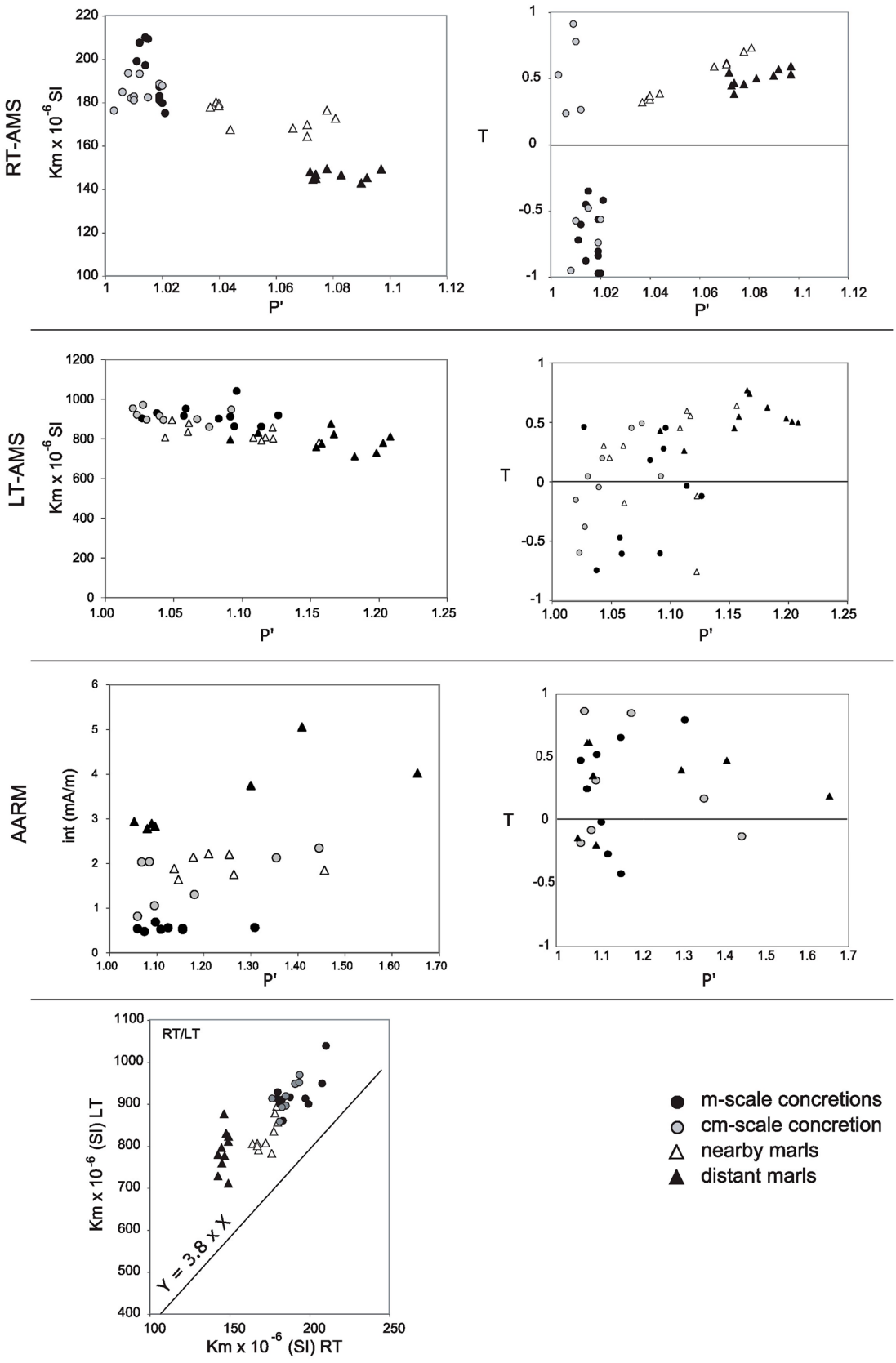
RT-AMS
Km x 10-6 SI
P'
T
LT-AMS
AARM
int (mA/m)
RT/LT
Km x 10-6 (SI) LT
Km x 10-6 (SI) RT
Y = 3.8 x X
m-scale concretions
cm-scale concretion
nearby marls
distant marls

◂**Fig. 3** Magnetic parameters: bulk magnetic susceptibility (Km), shape parameter (T) and anisotropic parameter (P') at room (RT and low (LT) temperatures AMS and AARM of every sample. At the bottom, the relationship of the magnetic susceptibility at low temperature respect to the room temperature (straight line represents the y = 3.8 × ratio, perfect paramagnetic)

the studied concretions and their sourrounding sediments, using SEM (Scanning Electron Microscope) equipped with and energy-dispersive x-ray imaging (EDS), and cathodoluminescence (CL), (which analyzes the radiation after an electron beam interacts with the rock, resulting in photons that are emitted in the ultraviolet to near-infrared region of the electromagnetic spectrum). Standard and polished thin-section of four selected samples were examined using optical and cathodoluminescence microscopes. (iv) Stable isotopic composition of selected samples provide information about the origin of the authigenic concretions.

3.1 Sampling and magnetic fabric and subfabric analyses

In order to better characterize magnetic fabric of the carbonate concretions and their host sediments, 11 specimens were collected from metric-scale concretions, 10 specimens from the centimetric-scale concretions, 10 specimens from the grey marls located in close vicinity (< 10 cm) to the concretions at the same stratigraphic horizon (when possible) and 10 specimens from the grey marls located few meters higher in the section from the horizons where the concretions appear (distant marls in Fig. 2). Sampling was done with a gasoline powered drill machine, refrigerated with water. Samples were oriented with a magnetic compass mounted on an orienting fixture. Bedding and slickensides on the bedding plane due to flexural folding were measured with a magnetic compass.

The samples were cut and the standard specimens (cylinders of ~ 2.1 cm height, ~ 2.5 cm diameter) were analyzed for the room temperature AMS (RT-AMS) at the paleomagnetic laboratory of the University of Barcelona-CSIC (GEO3BCN), in a KLY-2 (AGICO, Inc.), manually with 15 directional susceptibility measurements. Magnetic susceptibility is described by M = K * H (M is induced magnetization, K is the magnetic susceptibility and H the applied magnetic field). At room temperature the crystallographic preferred orientation, shape and composition with the distribution-interaction of magnetic minerals, are the factors controlling AMS (Tarling and Hrouda, 1993). The RT-AMS is a second rank tensor that is depicted by a three-axes ellipsoid ($k_{max} \geq k_{int} \geq k_{min}$). The shape and degree of magnetic fabric is quantified by other parameters deduced from the magnitudes of the axes of the ellipsoids: magnetic lineation ($L = k_{max}/k_{int}$), magnetic foliation ($F = k_{int}/k_{min}$); the corrected anisotropy degree, P' which indicates the intensity of the preferred orientation of minerals, the parameter of the anisotropy degree P (k_{max}/k_{min}) and the shape parameter T, indicating prolate fabrics when $-1 < T < 0$ and oblate when $0 < T < 1$ (Jelinek, 1981). The RT-AMS provides an averaged out fabric derived from the contribution of all magnetic minerals (paramagnetic, diamagnetic and ferromagnetic) present in the rock. In particular, Jelinek (1981) proposes the used of logarithms of the principal susceptibilities and their scattering. As a measure of the scatter of the logarithms of the principal susceptibilities, he suggested the factor P', (or Pj); P' = exp squareroot{$2[(n_1 - n)^2 + (n_2 - n)^2 + (n_3 - n)^2]$ }, where $n = (n_1 + n_2 + n_3)/3$ and n_1, n_2, n_3 are the logarithm of k_{max}, k_{int} and k_{min} respectively. P values from LT-AMS and AARM have been transformed to P' using the T values, following Jelinek (1981) as

$$P' = P^{\alpha}\left(\alpha = \text{square - root}\left(1 + T^2/3\right)\right)$$

Low temperature AMS (LT-AMS) analyses were done at the paleomagnetic laboratory of the University of Michigan using a SI2B susceptometer (Sapphire instruments) in 39 samples (out of the total 41 measured at RT-AMS). Samples were cooled down with liquid nitrogen (77 K) for 1 h before the magnetic susceptibility was measured. Six different measurements of the magnetic susceptibility were analyzed in six different directions while the sample is in a dewar with liquid nitrogen (Girdler, 1961). The paramagnetic susceptibility at low temperature is enhanced following the Curie–Weiss Law. An increase of the susceptibility at low temperature of 3–5 times the susceptibility at room temperature indicates the dominance of paramagnetic carriers in the AMS analyses (Parés & van der Pluijm, 2002), in those cases, the LT-AMS provides the preferred orientation of paramagnetic minerals.

The Anisotropy of the Anhysteretic Remanence Magnetization (AARM) was analyzed for 5–9 specimens per site using a SI-4 AF demagnetizer (Sapphire Instruments) at the paleomagnetic laboratory of the University of Michigan. Samples were subjected to an AF demagnetizing peak field of 100 mT while a 0.05 mT direct field was applied in a window of 5–50 mT. The window was chosen after partial Anhysteretic Remanent Magnetization measurements (pARM), and corresponds to the window range containing the highest pARM (Jackson et al., 1988). The AARM analyses were performed in nine different axes for every sample, measuring the remanent magnetization for every position in a 2G-cryogenic magnetometer at the University of Michigan. After each measurement, the sample was demagnetized along three orthogonal directions with an AF peak field of 100 mT. The computation of the AARM ellipsoid, which enables identification of the ferrimagnetic subfabric, was done using the Magnetic Anisotropy Analyses 3.1 (ARMA.

Table 1 Values of the scalar and tensorial properties at room temperature magnetic fabric ellipsoid

RT-AMS		Sample	Km (10^{-6} SI)	T	P'
m-scale concretions	BJB	1a	207.71	-0.602	1.012
	BJB	2a	197.29	-0.875	1.014
	BJB	2b	199.17	-0.718	1.011
	BJB	3a	210.13	-0.449	1.014
	BJB	3c	209.36	-0.348	1.015
	BJB	4a	183.1	-0.562	1.019
	BJB	4b	175.18	-0.418	1.021
	BJB	5a	181.24	-0.837	1.019
	BJB	5c	182.48	-0.971	1.019
	BJB	6a	187.53	-0.804	1.019
	BJB	6b	179.86	-0.971	1.020
cm-scale concretions	BJB	7a	176.4	0.529	1.003
	BJB	8a	182.16	0.914	1.009
	BJB	9a	182.9	0.780	1.010
	BJB	10a	185.02	0.239	1.006
	BJB	11a	188.7	-0.737	1.019
	BJB	111c	187.9	-0.563	1.020
	BJB	12a	182.56	-0.476	1.015
	BJB	13a	181.18	-0.574	1.010
	BJB	14b	193.63	-0.948	1.008
	BJB	15a	193.36	0.266	1.012
Marls far from concretions	BJM	1a	147.93	0.545	1.072
	BJM	1c	144.93	0.382	1.074
	BJM	2b	146.61	0.498	1.083
	BJM	2c	149.39	0.455	1.078
	BJM	3a	146.89	0.465	1.074
	BJM	3b	144.49	0.446	1.073
	BJM	5c	142.79	0.520	1.090
	BJM	6a	145.25	0.568	1.092
	BJM	7b	149.27	0.592	1.097
	BJM	8b	149.18	0.531	1.097
Marls near concretions	LB	1a	176.34	0.702	1.078
	LB	1b	172.58	0.732	1.081
	LB	2a	168.12	0.589	1.066
	LB	2b	164.36	0.616	1.071
	LB	2c	169.64	0.607	1.071
	LB	3a	180.12	0.340	1.039
	LB	4a	177.77	0.320	1.037
	LB	4b	179.49	0.340	1.040
	LB	4c	178.45	0.369	1.040
	LB	5a	167.44	0.385	1.044

Km bulk magnetic susceptibility, *T* shape parameter,*P'* corrected anisotropy degree

exe); the % of anisotropy was calculated as $(k_{max} - k_{min})/k_{mean}$ (McCabe et al., 1985). The anisotropy tensor was calculated by the least-squares method (Girdler, 1961). Isothermal Remanent Magnetizations of three axes saturated at different fields (IRM-three components, Lowrie, 1990) were done in order to identify the ferromagnetic *s.l.* carrier of the AARM and it is accompanied by the partial ARM.

The AARM shows the anisotropy of the low coercivity ferromagnetic minerals present in the rock. This methodology for the study of magnetic subfabrics has been successfully applied in the Pyrenean rocks to the north and east of the study area (Oliva-Urcia et al., 2009; Pueyo-Anchuela et al., 2010; Izquierdo-Llavall et al., 2015 and references therein) were a secondary ferromagnetic fabric was only detected by AARM to the original fabric (mostly paramagnetic).

3.2 Scanning Electron microscope (SEM) and cathodoluminescence (CL)

Observations of the mineralogy were done with a back scattered electron microscope Quanta-200 (SEM) at 20 kV at the University of Barcelona in samples BJB11, LB1 and BJM7 (metric scale concretion, nearby marls and distant marls from concretion, respectively). Qualitative chemical/elemental analyses (energy-dispersive X-ray spectroscopy; EDS) were performed with EDAX-Genesis software over four thin sections. Cathodoluminescence (CL) was also analyzed in m-scale concretion. A Technosyn Cold Cathodoluminescence Model 8200 Mk II operating at 16 ± 19 kV and 350 µA gun current was used.

3.3 Stable isotope analyses

Carbon and oxygen stable isotopic composition of four micro-drilled samples from microcrystalline carbonate matrix, carbonate cement and shells were measured from a concretion. The samples have been run on a Thermo-Finnegan Gas Bench II and a Delta Plus XP isotope ratio mass spectrometer at Geology and Geophysics Department, Texas A&M University. The isotopic data are reported relative to the Vienna-PDB standard. The laboratory precision is +/− 0.03‰ for **δ**13C and 0.05‰ for **δ**18O.

4 Results

4.1 Magnetic fabric and subfabric

4.1.1 Room-temperature AMS

Magnetic susceptibility ranges from 140 to 210 ($\times 10^{-6}$ SI) (average ~ 174, standard deviation ~ 19×10^{-6} SI). The values show a narrow range for the marls samples with the lowest values for the distant marls (144 to 149×10^{-6} SI) and 164 to 180 ($\times 10^{-6}$ SI) for the nearby marls. The concretions show the highest values of susceptibility from 176 to 193 ($\times 10^{-6}$

Table 2 Values of the scalar and tensorial properties at low temperature (77 K) magnetic fabric ellipsoid

LT-AMS	Sample	K mean (E−6)	T parameter	P ($K_{ma}x/K_{min}$)	$P' = P^{\alpha}$ (Jelinek, 1981)
m-scale concretions	BJB-1A	950	−0.607	1.056	1.059
	BJB-2A	914	−0.470	1.055	1.057
	BJB-2b	901	0.460	1.026	1.027
	BJB-3A	1039	0.453	1.093	1.096
	BJB4A	861	0.277	1.093	1.094
	BJB4a	860	−0.037	1.114	1.114
	BJB-4B	900	0.181	1.082	1.083
	BJB-5A	911	−0.602	1.086	1.091
	BJB-6A	917	−0.121	1.126	1.127
	BJB-6B	929	−0.746	1.035	1.038
cm-scale concretions	BJB11A	946	0.046	1.092	1.092
	BJB-7a	914	−0.046	1.040	1.040
	BJB-9a	895	0.044	1.030	1.030
	BJB-10a	897	0.451	1.065	1.067
	BJB-10a	920	−0.597	1.022	1.023
	BJB-12a	893	0.199	1.042	1.043
	BJB-13a	859	0.489	1.073	1.076
	BJB-14b	970	−0.379	1.027	1.028
	BJB-15a	952	−0.153	1.020	1.020
Marls far from concretions	BJM-1A	830	0.260	1.110	1.112
	BJM-1c	796	0.429	1.089	1.091
	BJM-2B	876	0.769	1.150	1.165
	BJM-2c	822	0.740	1.153	1.167
	BJM-3a	776	0.548	1.150	1.158
	BJM-5c	779	0.504	1.194	1.203
	BJM-5c	728	0.531	1.189	1.198
	BJM-6a	758	0.451	1.149	1.154
	BJM-7b	711	0.624	1.171	1.182
	BJM-8b	811	0.497	1.199	1.208
Marls near concretions	LB-1a	782	0.639	1.146	1.156
	LB-1b	807	0.553	1.111	1.117
	LB-2a	790	0.597	1.108	1.114
	LB-2b	805	0.452	1.105	1.108
	LB-3a	856	−0.757	1.112	1.122
	LB-4a	834	0.305	1.059	1.060
	LB-4b	894	0.202	1.048	1.049
	LB-4c	878	−0.178	1.061	1.061
	LB5a	806	0.304	1.043	1.044
	LB-5a	800	−0.121	1.122	1.123

K bulk magnetic susceptibility, *T* shape parameter, *P* anisotropy degree, and *P'* corrected anisotropy degree

SI) in the cm-scale concretions and 175–210 ($\times 10^{-6}$ SI) for the metric-scale concretion (Fig. 3, Table 1).

The corrected anisotropy degree (P') values are clustered for the concretion samples in one group with the lowest values (< 1.020) and the distant marls with the highest (1.070–1.100). Nearby marls show intermediate values between these two groups (Fig. 3). Shape parameter (T, varying between −1 and 1) reveals the prolate shape of all metric scale concretion samples and three cm-scale concretion samples (T < 0), being the rest of the samples oblate (T > 0). All these values fall within the range of magnetic susceptibility variability expected from previous paleomagnetic, AMS and rock magnetism studies in the Bartonian and Lutetian marls in the western Pyrenees (Larrasoaña et al., 2003, 2004; Pueyo-Anchuela et al., 2010, 2011) except

Table 3 Values of the scalar and tensorial properties of the ferrimagnetic ellipsoid. % of anisotropy (($k_{max} - k_{min}$)/k_{mean}), total intensity in mA/m, T: shape parameter and P: anisotropy degree obtained with ARMA excel calculations (McCabe et al., 1985) and P' as in Jelinek (1981)

AARM	Sample	%anisot	Total intensity (mA/m)	T	P	$P' = P^{\alpha}$ (Jelinek, 1981)
m-scale concretions	BJB-1a	11.151	0.568	0.799	1.277	1.309
	BJB-2a	12.976	0.542	0.658	1.145	1.155
	BJB-3a	8.739	0.689	0.525	1.093	1.098
	BJB-4a	11.722	0.558	−0.266	1.123	1.124
	BJB-4b	10.278	0.523	−0.011	1.109	1.109
	BJB-5a	14.644	0.515	−0.424	1.151	1.156
	BJB-6a	5.442	0.540	0.477	1.057	1.060
	BJB-6b	6.983	0.480	0.252	1.074	1.074
cm-scale concretions	BJB-11a	8.864	1.052	0.318	1.094	1.096
	BJB-9a	37.806	2.343	−0.126	1.444	1.445
	BJB-10a	29.517	2.124	0.173	1.352	1.354
	BJB-12a	5.814	0.814	−0.178	1.059	1.060
	BJB-13a	14.028	1.305	0.852	1.161	1.181
	BJB-14b	5.785	2.030	0.869	1.061	1.068
	BJB-15a	8.198	2.034	-0.076	1.085	1.085
Marls far from concretions	BJM-1a	8.273	2.900	0.357	1.088	1.089
	BJM-1c	7.024	2.787	0.619	1.075	1.079
	BJM-2b	9.203	2.835	−0.190	1.095	1.096
	BJM-2c	23.862	2.942	−0.136	1.052	1.052
	BJM-3a	70.481	2.585	0.776	2.706	2.977
	BJM-5c	24.299	3.754	0.405	1.291	1.300
	BJM-6a	24.299	3.754	0.405	1.291	1.300
	BJM-7b	30.643	5.065	0.479	1.391	1.409
	BJM-8b	48.131	4.027	0.196	1.649	1.654
Marls near concretions	LB-1a	106.1	3.377	0.670	5.465	6.179
	LB-1b	139.18	3.119	−0.397	2.923	3.005
	LB-2a	19.126	2.220	−0.011	1.210	1.210
	LB-2b	29.387	1.851	0.849	1.402	1.456
	LB-3a	13.19	1.643	0.282	1.144	1.146
	LB-4a	23.034	2.207	-0.180	1.252	1.254
	LB-4b	23.858	1.761	-0.177	1.262	1.264
	LB-4c	15.768	2.146	0.297	1.175	1.178
	LB-5a	11.852	1.888	0.548	1.130	1.137

for the conspicuous prolate shape data ($T < 1$) found within the concretions.

4.1.2 Low temperature AMS

Low temperature magnetic susceptibility values increase by a factor between 4.5 and 5.9 with respect to the magnetic susceptibility at room temperature (Fig. 3 at the bottom, Table 2) (larger than expected, since the increased value for a standard paramagnetic grain is 3.8, see Parés & van der Pluijm, 2002 and references therein) indicating mainly paramagnetic grains (probably phyllosilicates, ferroan carbonates, or pyrite, as seen under the microscope and explained in a later section) as the carriers of the magnetic susceptibility. The values range between 700 and 1000×10^{-6} SI. The anisotropy degree (P) and the corrected anisotropy degree (P') at low temperature increase respect to the corrected anisotropy degree (P') at room temperature due to the differential increase of k_{max} and k_{min} axes at low temperature (Parés & van der Pluijm, 2002). As seen in the methodology, P is the ratio between k_{max} and k_{min} axes, and P' is a more sophisticated measured of the same property (Jelinek, 1981).

4.1.3 AARM

The AARM isolates the anisotropy of the low coercivity ferromagnetic minerals and the intensity of the remanence shows the lowest values in the concretion samples (< 1 mA/m for the m-scale concretion). The marls nearby the cm-scale concretion show similar values of the artificial remanence as the cm-scale concretions (≤ 2 mA/m), but the

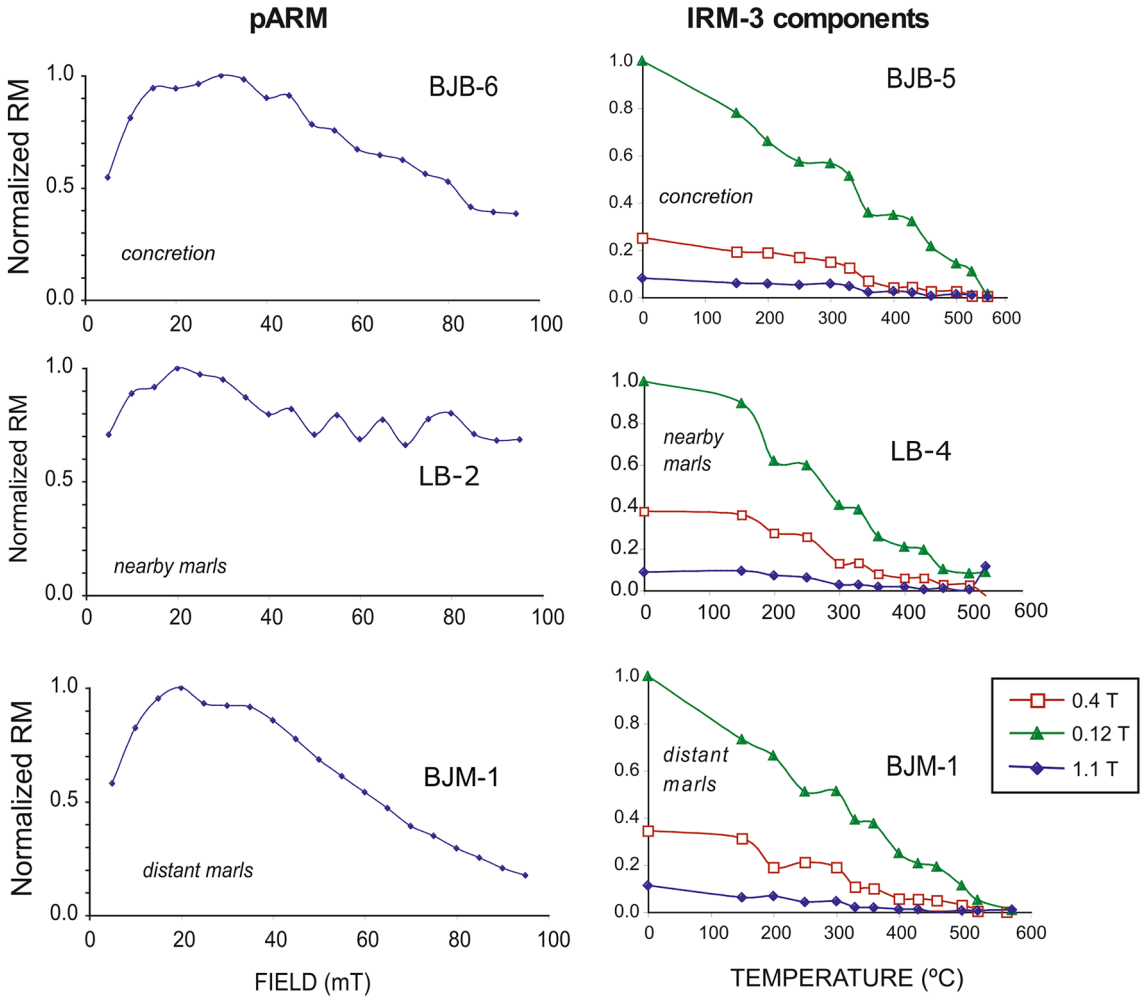

Fig. 4 On the left partial ARM curves showing the coercivity spectra of three selected samples. On the right, normalized intensity decay curves of the thermal demagnetization of the IRM of the three components (Lowrie test, 1990)

distant marls have higher values from 2.5 to 5 mA/m. Most of the samples show oblate shapes. Figure 3, Table 3.

4.1.4 Magnetic analyses (pARM and 3c-IRM)

The partial Anhysteretic Remanent Magnetization (pARM) shows the coercivity spectrum with a peak between 5 and 50 mT, a low coercivity mineral. In addition, demagnetization of the three artificial magnetizations perpendicularly applied (3 components Isothermal Remanent Magnetization) suggests that the AARM carrier is a soft coercive mineral with an unblocking temperature of 580 °C (magnetite) in the marls and concretions, but there is also a decay at ~ 320–340 °C related to ferromagnetic *s.l.* iron sulphides in the soft (green, 0.12 T) and medium (red, 0.4 T) coercivity axes, very clear in the BJB (carbonate concretions) and in the nearby (LM) and distant marls (BJM), names of sites as they appear in the tables (Fig. 4).

4.1.5 Orientation of the ellipsoids

At room temperature the concretion samples (BJB, BJM) show inverse fabrics, with k_{max} axes clustered at the pole of the bedding plane and k_{min} and k_{int} on the bedding plane (Fig. 5, Table 4). However, the marls samples (near and far from the concretions) show normal fabric at room temperature. The orientation of the axes in the concretion samples is similar and the same occurs in the two groups of marls.

The separation of the magnetic fabric at room temperature (RT-AMS) in subfabrics at low temperature (LT-AMS) and with the ferromagnetic fabric (AARM) provide information about the carriers of the subfabrics. On one hand, the RT-AMS and LT-AMS show the inverse fabric in the concretions, with larger scattering in the centimetric scale concretions. On the other hand, RT-AMS and LT-AMS remain similar and normal (k_{min} axes perpendicular to bedding) in the marls, with higher scattering in LT-AMS in the

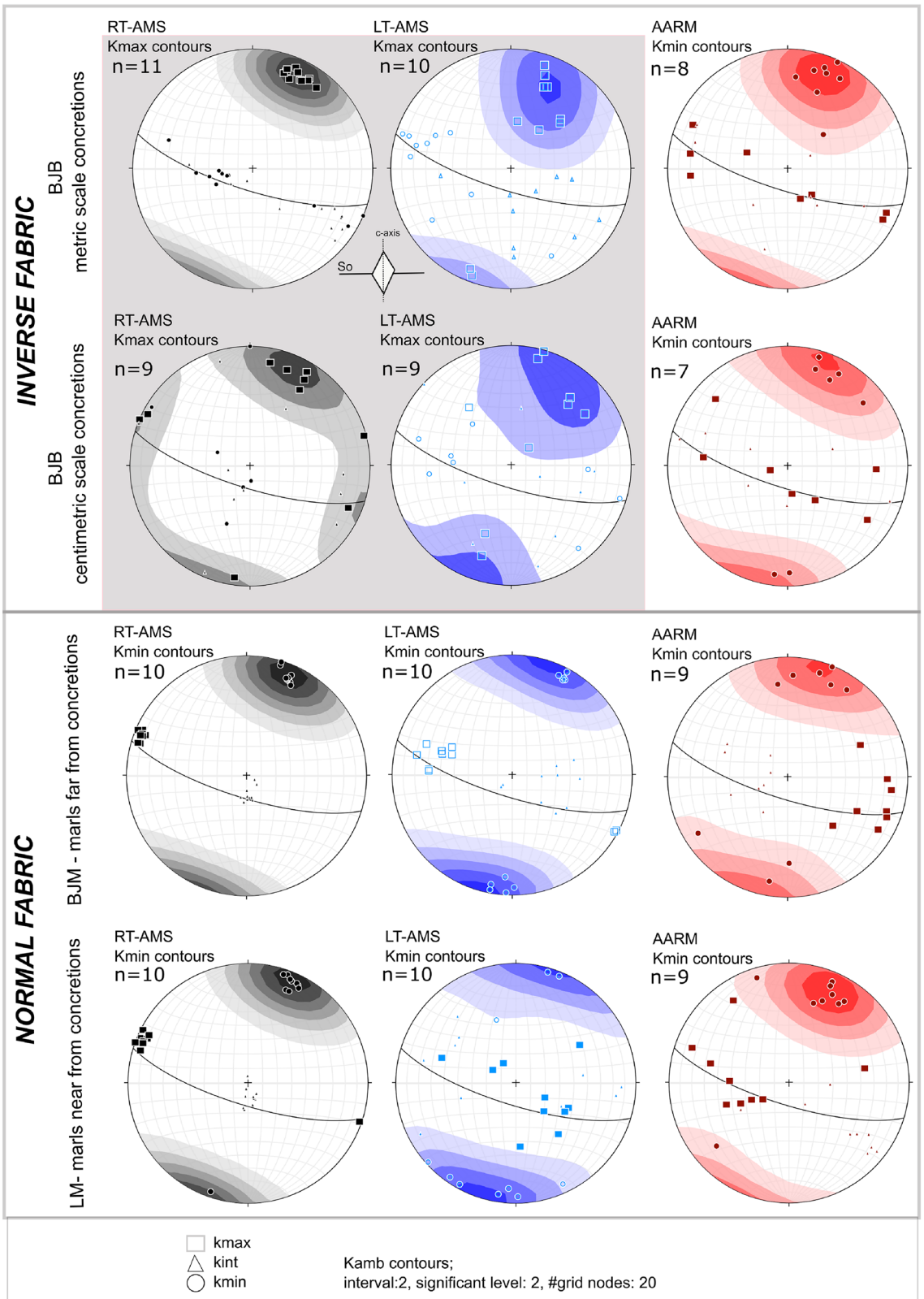

nearby marls. However, in both lithologies (concretions and marls), the ferromagnetic grains seem to orient normal with the bedding plane (normal fabric), so that the AARM shows normal fabric, with k_{max} and k_{int} axes distributed on the bedding plane and the k_{min} axes located at the pole to the bedding plane. The different behavior of the magnetic fabrics

◂**Fig. 5** Stereographic projection (lower hemisphere) in geographical coordinates of the three axes of the magnetic fabric ellipsoid at room temperature (left), low temperature (center) and AARM (right). Notice that for the stereoplots with a grey background, the contours are for the maximum axes (k_{max}), the other stereoplots are representing the contours for the k_{min} axes. The great circle in black is the bedding plane (107, 75 S). The slickensides found on the bedding planes, due to flexural folding are: 114, 77S; 76E (not represented). A carbonate crystal with the c-axis and bedding plane represents the orientation of the AMS at RT and LT in the concretions (following Hunslow, 2001)

between the concretions and the marls suggests different magnetic carriers of the petrofabric. The ferroan carbonates would be the carriers of the magnetic fabric at room and low temperature in the concretions, with the c-crystallographic axis perpendicular to bedding, whereas phyllosilicates (also paramagnetic) are the carriers of the magnetic fabric in the marls. In all cases, the ferromagnetic *s.l.* minerals, magnetite (and ferromagnetic *s.l.* iron sulphides) keep the same orientation in both the concretions and the marls, slightly best clustered in the marls for the k_{max} and k_{int} axes.

4.2 Microscope (SEM) observations

The concretions are almost solely composed by euhedral dolomite crystals with an iron enriched border (Fig. 6, with larger Fe content in the border sample). Most grains show the rombohedral shape typical of dolomite. The marls are mainly composed by calcite, quartz, phyllosilicates (mica, chlorite, intergrown *phyllosilicates*) and framboids of iron sulphides (pyrite). The marls near the concretions (less than 10 cm) are similar to the marls far from the concretions but contain some dolomite crystals (15%). As accessory minerals there are apatite, phosphates, sphene, albite, Ti-oxides and rare earth-bearing minerals.

Dolomite in the concretions is very homogeneous in crystal size, 5 to 20 µm. Exceptionally two bands of growth with a border enriched with iron is found (Fig. 6.a). Phyllosilicate grain size ranges from 10 to 60 µm. Framboids of iron sulphides can reach 100 µm. Euhedral grains of iron sulphides are also found within the phyllosilicates layers.

Cathodoluminescence enhances the Fe-rich rim in the dolomite crystals, with different red tone. It is particularly well observed in BJB sample (Fig. 7, right column).

4.3 Stable isotope analyses

The values obtained for the four samples vary from near zero in both isotopes (C and O) for the carbonate concretions, and smaller values (depleted in heavy isotopes, that is, more negative values) for the marly samples (Table 5).

5 Discussion

5.1 Magnetic properties and inverse magnetic fabrics

The magnetic analyses performed in the carbonate concretions and surrounding marls at the top of the Eocene flysch sediments in this part of the South Pyrenean Zone allow to determining that: (i) the RT- and LT-AMS carriers are paramagnetic minerals, as evidenced by the large increase in magnetic susceptibility at low temperature, with no significant changes in the orientation of the k_{max} axes between RT- and LT-AMS magnetic fabric ellipsoids. However, the main carrier differs between the carbonate concretions and the marls. In the marls, both the RT-AMS and the LT-AMS are normal, that is, with the k_{min} axes perpendicular to bedding, whereas the carbonate concretions show a *simple inverse* fabric according to Cerny et al. (2020) and references therein, with the k_{max} axes perpendicular to bedding, as is represented in the first model of Hunslow (2001) (his Fig. 14A) or in the right corner of the ternary diagram of Chadima et al. (2006) and references (their Fig. 6). There is a larger scattering of the magnetic axes (k_{max} particularly) at LT-AMS (and also at RT-AMS) in the concretions than in the marls. The scattering of crystallographic c-axes of siderite within the different siderite phases in the concretion has been proposed to provide different types of magnetic fabrics in the very detailed study of Hounslow (2001). In our study, we cannot discard some c-axes scattering, but the ferroan dolomite crystals seem to be perpendicular to the bedding plane, resulting in prolate shapes of the magnetic fabric ellipsoid (at RT-AMS and for most samples at LT-AMS, Fig. 3).

The microscope observations allow distinguishing between the paramagnetic carriers: in the carbonate concretions is the Fe-rich dolomite, and in the marls are the phyllosilicates. Furthermore, different Fe concentration in concentric rings can be observed in the Fe-rich dolomite by means of both SEM and cathodoluminescence, which indicates evolving pore waters where the concentrations of dissolved iron shifted in time. We cannot distinguish different orientations of the ferroan carbonates, as Hunslow (2001) did in his research within the siderite phases, but maybe some scattering of the magnetic ellipsoid in the concretions is related to the different chemical composition in our samples.

The c-crystals perpendicular to bedding plane are similar as in Fig. 14A of Hounslow (2001), or in the right corner of the ternary diagram presented in Chadima et al (2006) (Fig. 6 in that study). We do not see the effect of a flow in the analyzed sediments.

Table 4 Declination (DEC) and inclination (INC) in geographic coordinates of the axes of the magnetic fabric ellipsoid at room (RT-AMS) and low (LT-AMS) temperatures as well as the anisotropy of the anhysteretic remanent magnetization (AARM)

	RT-AMS		Kmax		Kint		Kmin		LT-AMS	Kmax		Kint		Kmin		AARM	Kmax		Kint		Kmin	
			DEC	INC	DEC	INC	DEC	INC		DEC	INC	DEC	INC	DEC	INC		DEC	INC	DEC	INC	DEC	INC
m-scale concretions	BJB	1a	23	9	205	81	113	0	BJB-1a	18	10	132	67	284	20	BJB-1a	292	60	116	30	25	2
	BJB	2a	28	17	146	57	289	27	BJB-2a	20	18	182	72	288	6	BJB-2a	157	68	296	17	30	14
	BJB	2b	22	20	119	17	247	63	BJB-2b	45	41	264	41	155	21	BJB-3a	137	66	286	21	20	11
	BJB	3a	32	12	124	11	255	73	BJB-3a	47	43	178	34	287	28	BJB-4a	279	19	141	65	15	16
	BJB	3c	32	14	127	19	267	67	BJB-3c	36	57	178	27	277	17	BJB-4b	266	20	141	58	5	24
	BJB	4a	25	12	118	17	261	69	BJB-4a	24	26	177	61	288	12	BJB-5a	295	14	196	31	46	56
	BJB	4b	19	15	116	25	260	60	BJB-4b	200	6	100	58	294	32	BJB-6a	118	11	224	56	21	32
	BJB	5a	38	15	131	10	255	72	BJB-5a	22	27	120	16	237	58	BJB-6b	114	11	59	72	22	15
	BJB	5c	29	17	235	72	121	8	BJB-6a	8	57	137	23	237	23							
	BJB	6a	18	17	120	34	266	51	BJB-6b	202	11	100	47	301	41							
	BJB	6b	19	13	274	46	121	40														
cm-scale concretions	BJB	7a	188	7	95	23	293	66	BJB11a	43	31	250	56	141	12	BJB-11a	141	60	292	27	29	13
	BJB	8a	21	15	291	1	198	75	BJB-7a	201	39	10	50	107	6	BJB-9a	257	78	109	11	16	6
	BJB	9a	75	2	344	10	176	80	BJB-9a	198	22	94	31	317	51	BJB-10a	92	27	295	62	187	10
	BJB	10a	297	5	32	43	202	47	BJB-10a	324	40	206	28	93	36	BJB-12a	313	19	181	63	50	19
	BJB	11a	32	16	195	73	301	5	BJB-10a	14	9	111	38	273	50	BJB-13a	171	71	284	8	16	17
	BJB	111c	33	25	206	65	302	3	BJB-12a	41	26	148	31	279	48	BJB-14b	124	21	244	60	26	21
	BJB	12a	31	9	124	14	268	73	BJB-13a	55	54	165	14	264	32	BJB-15a	276	30	69	57	179	12
	BJB	13a	11	13	107	22	253	64	BJB-14b	16	1	111	69	286	21							
	BJB	14b	293	0	203	4	25	86	BJB-15a	45	73	313	1	223	17							
	BJB	15a	113	12	260	75	21	8														
Marls far from concretions	BJM	1a	292	10	166	73	24	14	BJM-1a	274	31	90	59	183	2	BJM-1a	120	14	249	69	25	16
	BJM	1c	293	4	179	80	24	9	BJM-1c	289	46	93	43	191	8	BJM-1c	109	14	252	73	17	10
	BJM	2b	287	8	130	81	17	4	BJM-2b	273	31	78	59	179	7	BJM-2b	116	36	253	49	3	16
	BJM	2c	287	6	115	84	17	1	BJM-2c	282	20	92	70	191	3	BJM-2c	66	34	299	42	179	29
	BJM	3a	293	7	178	74	25	15	BJM-3a	287	39	76	46	184	16	BJM-3a	112	12	286	78	22	1
	BJM	3b	294	6	186	72	26	17	BJM-4c	118	2	224	81	28	9	BJM-5c	97	14	321	71	190	13
	BJM	5c	293	2	195	75	23	14	BJM-5c	119	3	223	79	29	10	BJM-6a	97	14	322	71	238	13
	BJM	6a	292	7	173	75	23	13	BJM-6a	290	25	133	63	25	9	BJM-7b	137	44	292	43	34	13
	BJM	7b	291	8	167	75	23	12	BJM-7b	295	44	121	46	28	3	BJM-8b	91	18	215	61	354	23
	BJM	8b	291	6	178	76	22	13	BJM-8b	289	38	131	50	28	11							

Table 4 (continued)

	RT-AMS		Kmax		Kint		Kmin		LT-AMS	Kmax		Kint		Kmin		AARM	Kmax		Kint		Kmin	
			DEC	INC	DEC	INC	DEC	INC		DEC	INC	DEC	INC	DEC	INC		DEC	INC	DEC	INC	DEC	INC
Marls near concretions	LB	1a	291	4	188	72	22	17	LB-1a	300	72	97	17	189	7	LB-1a	326	18	92	62	229	21
	LB	1b	293	4	191	73	24	17	LB-1b	289	35	117	55	22	4	LB-1b	290	15	143	72	23	9
	LB	2a	109	2	357	85	199	5	LB-2a	328	74	92	13	184	13	LB-2a	79	36	241	52	343	9
	LB	2b	290	0	198	86	20	4	LB-2b	276	46	83	43	179	6	LB-2b	251	44	127	30	17	31
	LB	2c	287	7	141	81	18	5	LB-3a	140	44	242	11	343	44	LB-3a	238	69	128	8	34	19
	LB	3a	297	2	191	81	27	9	LB-4a	115	50	302	40	209	4	LB-4a	246	62	128	14	32	23
	LB	4a	294	9	156	78	26	8	LB-4b	120	51	309	39	215	5	LB-4b	247	54	123	22	22	27
	LB	4b	292	7	159	79	23	8	LB-4c	135	63	319	27	228	2	LB-4c	272	49	130	34	26	19
	LB	4c	296	9	168	75	28	11	LB5a	116	68	284	22	16	4	LB-5a	284	33	132	13	23	13
	LB	5a	291	7	159	80	22	7	LB-5b	59	38	255	51	155	8							

Interestingly, the low coercivity ferromagnetic *s.l.* mineral present keeps the same orientation in all samples (carbonate concretions and marls). This orientation is normal, with the k_{min} axes perpendicular to bedding. (ii) The ferromagnetic *s.l.* mineral is magnetite and possibly some ferromagnetic *s.l.* iron sulphides as suggested by the three components IRM analyses. The fact that AARM shows the same orientation in both concretions and marls indicates that the ferroan carbonate is the inverse fabric carrier and not SD magnetite, since SD magnetite results in normal fabric when analyzed by AARM (Rochette, 1988).

5.2 Origin of concretions and magnetic fabric

Regarding the stable isotopic composition, we compare our results from the top of the prodeltaic Larrés Formation, deposited in a slope environment (Remacha et al., 2005) with other stable isotopic results from the Eocene Aínsa basin (Fig. 8), about 100 km to the East, closer to the proximal zone of the distributary system represented by the Sobrarbe delta (Hoareau et al., 2009; Mutti, 1977). These Eocene samples presented in Läuchli et al. (2021) come from concretions (with different shapes) and other lithologies (marls and calcite in fracture fills) (Hoareau et al., 2009) including marine carbonate mudstone. These authors sampled the finer and less deformed hemipelagic deposits at 30–40 cm below the weathering surface in three sections (Fig. 8).

Our results from the marls (BJM-7A and LB-1C) show similar values as the ones in the mudstones from the Aínsa basin (they locate near Forcaz, Labuerda and Morillo de Tou values). The stable isotopic results in the sections from the Aínsa basin have been used in order to decipher the climatic and/or eustatic contribution to sedimentation besides the tectonic input. The previous $\delta^{13}C$ and $\delta^{18}O$ values in the Aínsa basin are generally lower than their global marine equivalents (Eocene benthic marine foraminifera records of Cramer et al., 2009). In addition, information from calcite veins suggests some little diagenetic overprint on the studied deposits (Mansurbeg et al., 2009; Travé et al., 1997 in Läuchli et al., 2021).

These previous studies, suggest that the isotopic signal comes from the time of lithification, as micritic cement of marine origin, since mixing with meteoric water values found in calcite/dolomite veins would show scatterer values (Travé et al., 1997; Mansurbeg et al., 2009, in Läuchli et al,. 2021). Notwithstanding they cannot constrain time or depth for the lithification, they propose temperature lower than 50ºC for the concretions to form in the Sobrarbe delta (Hoareau et al., 2009). The variations along the sections are suggested to reflect the isotopic signal of the marine water, so the general trend toward more positive $\delta^{18}O$ values is explained by a gradual cooling as in the global record, whereas the $\delta^{13}C$ values of the Larrés Formation show

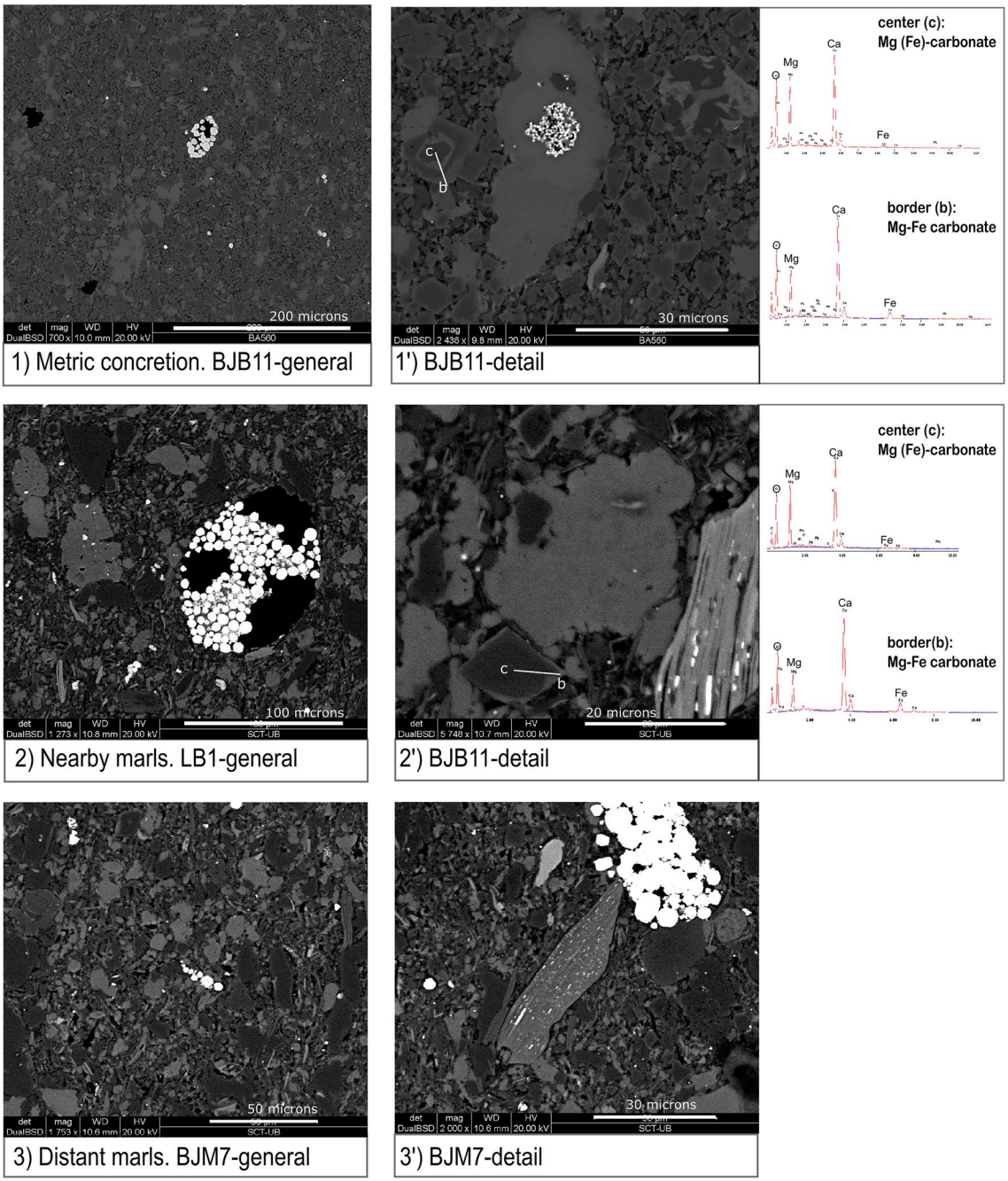

Fig. 6 General and detailed view of the concretions (1) and marls (2 and 3). SEM images with qualitative elemental analyses (EDS) allow distinguishing Mg-carbonate with Fe enriched rims (1 and 2), rhombohedral shapes are common. Scale is at the bottom right. Framboids of iron-sulphides are also present (1, 2 and 3). Large phyllosilicates show intergrown of Fe-sulphides (2′, 3′)

discrepancies with the global record of Cramer et al. (2009) and it is interpreted in relationship with sea level changes, as seen by Castelltort et al. (2017). This is plausible as long as there is no significant change in the environment of deposition and the authors remark that carbonates isotope composition responds relatively fast to sea-level changes (Läuchli et al., 2021 and references therein).

Regarding the results from the stable isotope of the carbonate concretions (BJB-11B and BJB-2C) with inverse fabric of our study, they are closer to the values of the small tubular concretions and some of the dolomitic concretions in the Aínsa basin, whose early diagenetic precipitation has been interpreted to occur before tilting of bedding, at burial depths shallower than 400 m and discarding a deep source

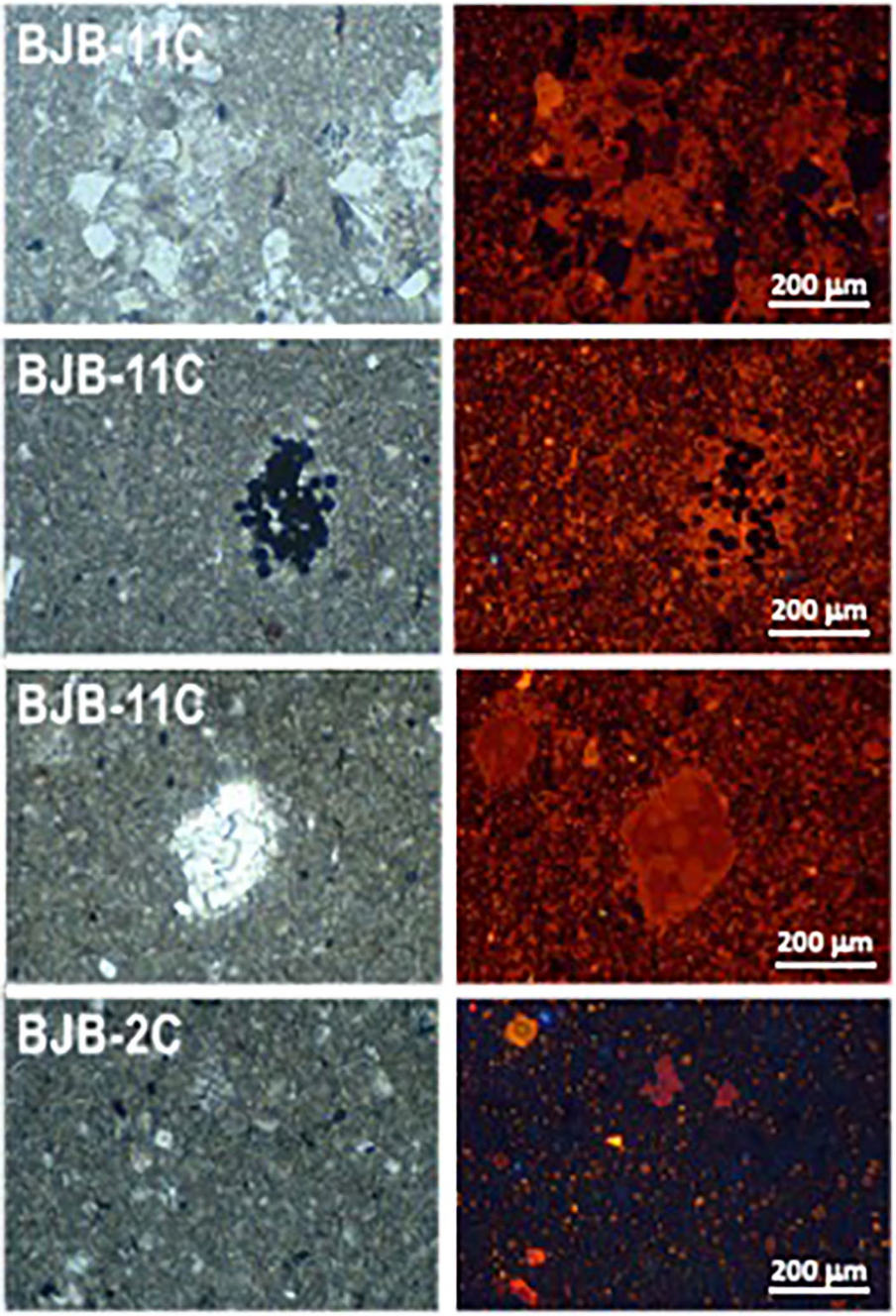

Fig. 7 Petrographic and cathodoluminescence photographs illustrating the different iron content in the dolomites for the carbonate concretions. Same scale for all thin sections

Table 5 Values of the stable isotopic composition

Sample	$\delta^{13}C\%$ (V-PDB)	$\delta^{18}O\%$ (V-PDB)
BJB 11B (m-scale concretion)	−0.36	−1.43
BJB 2C (cm-scale concretion)	0.15	0.02
BJM 7A (nearby marl)	−1.06	−4.48
LB-1C (distant marl)	−1.23	−4.13

Carbonate concretions: BJB, nearby marls: LB and distant marls: BJM. V-PDB is a standard value to compare values to, and originally it was the Vienna Pee Dee Belemnite (PDB) from the Peedee Fm.

for the fluid involved in their precipitation (data from Sr isotopes, mineralogical and petrographical analyses) (Hoareau et al., 2009). The development of the magnetic fabric in all lithologies agrees with a pre-tilting origin in a basin where layer-parallel shortening may affect the sediments during their deposition (see models in García-Lasanta et al., 2018). This is particularly clear for the RT-AMS, where k_{max} axes (k_{min} axes for the concretions) are parallel to the general structure of the syncline (~ENE-WSW), and k_{min} axes (k_{max} axes for the concretions) are perpendicular to the bedding

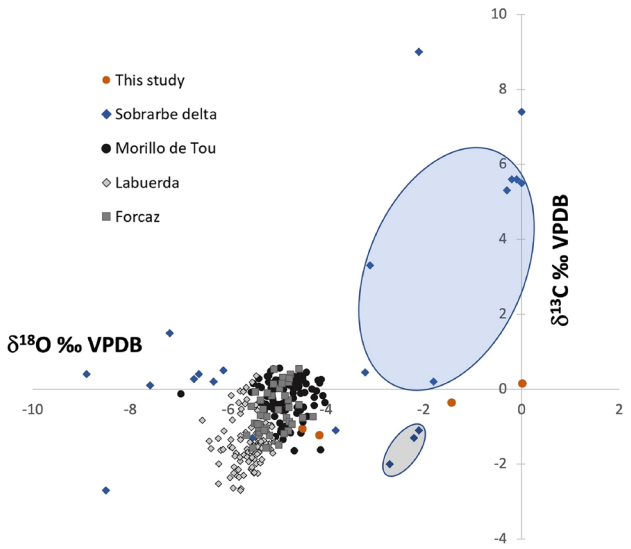

Fig. 8 Stable isotopic composition of individual samples (normalized VDP). In orange, results from this study, in blue, from Hoareau et al. (2009), which are from different types of carbonate concretions and marls in the Aínsa basin, and in grey and black results from marls in three sections (Morillo de Tou, Labuerda and Forcaz) in the Aínsa basin from Läuchli et al. (2021). The ellipse with grey background cluster the small tubular concretions, and the ellipse with blue background marks the dolomitic concretions (for more details, see Hoareau et al., 2009)

plane (Fig. 9). The marls show clearly this behavior, they have a tectonic fabric related to compression, probably the compression affects the minerals since the time of deposition, but the fabric is enhanced due to the later incorporation of the basin to the Pyrenean orogen, in the Izaga syncline. This fabric is more strained that the ones located in the surroundings (located in Fig. 1, from Larrasoaña et al., 2004), with all axes well grouped and accordingly to a NE-SW shortening direction.

Whereas in the concretions, the RT-AMS results of the cm-scale concretions show similar behavior to that of the marls, with a girdle distribution of axes in a WNW-ESE orientation and the metric scale concretions the k_{min} axes are located in a NE-SW orientation, instead of the Pyrenean orientation of ~ ENE-WSW due to layer parallel shortening and later coaxial compression. These would suggest that the carbonate concretion fabric predates the fabric from the marly rocks and that the phyllosilicates in the marly rocks are more sensitive to the compression than the carbonate concretions. In addition, the fabric of the phyllosilicate grains continues developing during burial diageneses, that is, the early mineralogical transformations of the Paleogene mudstones are accompanied by strong alignments of illite–smectite, while chlorite is formed and also align with detrital illite. The water released from the transformation of smectite to illite is suggested to act as a lubricant for further phyllosilicate grain alignment in the mudstones (Day-Stirrat et al., 2008). If there is some compression acting during the time of deposition, the Eocene is a tectonically active time in the Pyrenees (Muñoz, 1992; Teixell, 1998), a NE-SW compression can affect the developing fabric at burial diagenesis.

Concretions are usually hosted in fined-grained sedimentary rocks (shales, marls, mudstones) and formed by diffusion of a slow three-dimensional advection of water that involve carbonate inter-conversion reactions. Microbial processes can be important and crucial in the concretion formation. The factors to take into account are the decay rate of organic matter (OM), carbonate saturation, porewater velocity and rate of authigenic precipitation. Different mineralization reactions can occur, including silicification, phosphatization, pyritization or carbonate precipitation, although carbonates are the most commonly precipitated biominerals (Dhami et al., 2023 and references therein). Carbonate precipitations need high alkalinity in anaerobic conditions, where sulfate reduction H_2S, together with anaerobic methane oxidation and carbonate supersaturation (free calcium and carbonate ions) lead to carbonate precipitation, at high pH (6.38–7.2) (Dhami et al., 2023 and reference therein). So, for the formation of a ferroan carbonate in marine environments to occur, oxidation of organic matter has to take place in order to form bicarbonate ions. The sulfate reduction will provide pyrite when reacting with iron.

Once bacterial sulfate reduction ceases, the organic matter oxidation occurs by iron reduction and methanogenesis. This promotes iron carbonate precipitation. Carbonate concretion growth is proposed to proceed until the organic matter is exhausted (Dhami et al., 2023 and reference therein). Therefore, the limiting factors for the precipitation of the carbonate concretions would be the presence of bacteria and organic matter, considering that the S is present in the sea water and Fe can be provided by the siliciclastic input in the turbiditic basin. Relating the isotopic composition to environmental conditions such as temperature needs careful consideration and other type of data (i.e., Sr). It is interesting to note that massive production of dolostones is called the dolomite paradox, which reflects an apparent monotonic decrease in abundance relative to limestone since the Paleozoic. However, some authors argue that the stratigraphic distribution of dolostone reflects global scale perturbations of the Earth system that can be linked to variations in seawater geochemistry, some related to higher atmospheric pCO2 (references in Bruns et al., 2000), which contrasts with the diagenetic models that consider that Mg-rich fluid-rock interactions during burial contributed to the stratigraphic history of dolostones. At present, microbial films are related to the production of authigenic dolomite in large quantities (Petrash et al., 2017 and references therein).

In any case, the formation of authigenic carbonates demands sulphate-limited environments where

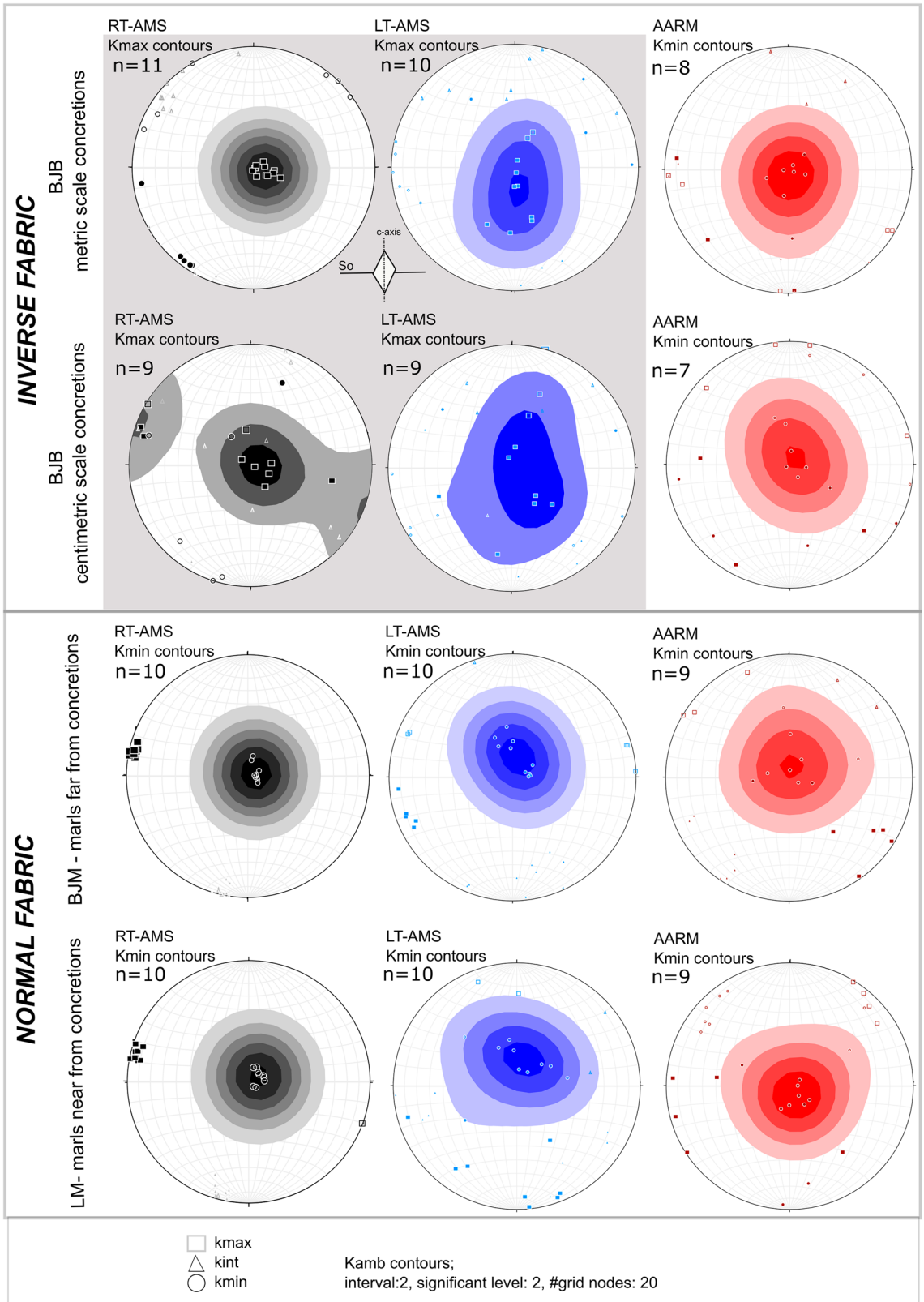

Fig. 9 Stereographic projection (lower hemisphere) when bedding is restored to horizontal of the three axes of the magnetic fabric ellipsoid at room temperature (left), low temperature (center) and AARM (right). Legend as in Fig. 5

methanogenesis takes place (Dhami et al., 2023 and reference therein); therefore, we interpret that the ferroan dolomitic concretions studied in this paper are linked to the supply of organic matter in amounts high enough to drive its degradation to the stage well beyond sulphate reduction, that is, to the point of carbon dioxide reduction and the concomitant production of methane. In this regard, it is important to note that the ferroan dolomitic concretions studied in this paper are not randomly distributed throughout the section, but are instead located at a specific position across the basin within the uppermost 400–250 m of the Larrés Formation. This formation accumulated in a slope environment in response to the progradation of the deltaic systems developed further east in the then emerged areas of the Central Pyrenees, and therefore provides the ideal context for explaining an enhanced supply of organic matter. Biostratigraphic data from across the Jaca-Pamplona basin (Canudo and Molina, 1988; Canudo et al., 1988; Payros et al., 1999; González-Lanchas et al., 2019) yield a lower Bartonian age for the upper part of the Larrés Formation, where the ferroan dolomitic concretions are found. Magnetostratigraphic data are available only for the eastern part of the basin, where the upper part of the Larrés Formation hosting the concretions has been dated to the uppermost part of chron C18r, at an age of around 40–40.5 Ma (Oms et al., 2003; Vinyoles et al., 2021). Noticeably, this time coincides with the Middle Eocene Climate Optimum (MECO), a prolonged period of global warming that left its imprint in the Jaca-Pamplona basin by inducing a rapid progradation of fluvial-deltaic sedimentary systems and a concomitant increase in the supply of terrestrial organic matter (Peris-Cabré et al., 2023). Here we propose that it is the increased supply of terrestrial organic matter during the MECO and its burial in prodeltaic marls of the Larrés Formation what drove diagenetic reactions to the point of methane formation and the authigenic growth of the studied ferroan dolomitic concretions. In this regard, the formation of these concretions does not only represent a potential additional sedimentological expression of the MECO, but also provide a mechanism for explaining its somehow enigmatic demise through sequestration of carbon from Earth's atmosphere (see Torres et al., 2020). Ongoing magnetobiostratigraphic results from exposed sedimentary successions in the Izaga syncline will enable disentangling the chronology of the Larrés Formation in the western part of the Jaca-Pamplona basin and its detailed correlation with its counterparts in the eastern part of basin. This will enable, in turn, to determine if the paleoclimatic significance assigned here to the studied ferroan dolomitic concretions (e.g., as an additional sedimentological expression of the MECO and a contributor to its demise) is correct or not.

6 Conclusions

The detailed study of the magnetic fabrics and subfabrics in 40 samples of the flysch deposits of the Jaca-Pamplona basin reveals the inverse character of the magnetic fabric in the authigenic carbonate concretions embedded in the flysch sediments. These inverse fabrics are characterized by the interchange between k_{max} and k_{min} axes in such a way that k_{min} axes are parallel to the synclinal axis whereas the k_{max} axes are perpendicular to the bedding plane.

A variation in the fabric is observed from the carbonate concretions through the cm-scale concretions, nearby marls to the distant marls. The optical and qualitative compositional analyses allows us to corroborate that the carrier of the magnetic inverse fabric observed in the carbonate concretions is ferroan dolomite with a mobile redox front. The tectonic type magnetic fabrics observed in the marls is most probably related to the compression during burial and it is enhanced during the inversion of the basin.

The authigenic carbonate concretions studied here show isotopic composition close to the tubular and dolomitic concretions of the Sobrarbe delta (Aínsa basin), between the tubular and the dolomitic concretions in the eastern side of the Aínsa basin, which are related to precipitation from marine water due to microbial activity during burial. Given the middle Eocene age of the deposits considered in this work, we relate the formation of the studied concretions to the period of global warming known as Middle Eocene Climate Optimum (MECO).

Acknowledgements Thanks to all researchers in the different magnetic laboratories for their technical and intellectual support, particularly the warm welcoming of Prof. Rob Van der Voo.

PID2021-12246NB-C22 funded by MICIU/AEI/https://doi.org/10.13039/501100011033 and by FEDER, UE and the Catalan Council to the Grup Consolidat de Recerca Reconegut Geologia Sedimentària (2021 SGR-Cat 00349).

Funding Open Access funding provided thanks to the CRUE-CSIC agreement with Springer Nature.

Data availability Data is available upon request to corresponding author.

Declarations

Conflict of interest On behalf of all authors, the corresponding author states that there is no conflict of interest.

References

Aloisi, G., Pierre, C., Rouchy, J. M., Foucher, J. P., & Woodside, J. (2000). Methane-related authigenic carbonates of eastern Mediterranean Sea mud volcanoes and their possible relation to gas hydrate destabilisation. *Earth and Planetary Science Letters, 184*(1), 321–338.

Borradaile, G. J., & Jackson, M. (2010). Structural geology, petrofabrics and magnetic fabrics (AMS, AARM, AIRM). *Journal of Structural Geology, 32*(10), 1519–1551.

Boya, S. (2019). El Sistema deltaico de la Arenisca de Sabiñánigo y la continentalización de la cuenca de Jaca, 207 p. PhD thesis. ISBN 9788449083006.

Burns, S. J., & McKenzie, J. A. V. (2000). Dolomite formation and biogeochemical cycles in the Phanerozoic. *Sedimentology, 47*(2000), 49–61.

Canudo, J. I., & Molina, E. (1988). Biocronología con foraminíferos planctónicos de la secuencia deposicional de Jaca (Pirineo aragonés): Eoceno medio y superior. In *Actas II Congreso Geológico de España*, *1*, 273–276.

Canudo, J. I., Molina, E., Riveline, J., Serra-Kiel, J., & Sucunza, M. (1988). Les événements biostratigraphiques de la zone Prépyrénéenne d'Aragon (Espagne), de l'Éocene moyen à l'Oligocene inférieur. *Révue de Micropaléontologie*, *31*(1), 15–29.

Casas, A. M. (2005). C. Sismicidad inducida por el embalse de Itoiz. Informe.

Castelltort, S., Honegger, L., Adatte, T., Clark, J. D., Puigdefàbregas, C., Spangenberg, J. E., Dykstra, M. L., & Fildani, A. (2017). Detecting eustatic and tectonic signals with carbon isotopes in deep-marine strata, Eocene Ainsa Basin, Spanish Pyrenees. *Geology, 45*(8), 707–710.

Černý, J., Melichar, R., Všianský, D., & Drahokoupil, J. (2020). Magnetic anisotropy of rocks: a new classification of inverse magnetic fabrics to help geological interpretations. *Journal of Geophysical Research: Solid Earth, 125*(11), e2020JB020426.

Chadima, M., Pruner, P., Šlechta, S., Grygar, T., & Hirt, A. M. (2006). Magnetic fabric variations in Mesozoic black shales, Northern Siberia, Russia: Possible paleomagnetic implications. *Tectonophysics, 418*(1–2), 145–162.

Coleman, M. L. (1993). Microbial processes: Controls on the shape and composition of carbonate concretions. *Marine Geology, 113*, 127–140.

Cramer, B. S., Toggweiler, J. R., Wright, J. D., Katz, M. E., & Miller, K. G. (2009). Ocean overturning since the Late Cretaceous: Inferences from a new benthic foraminiferal isotope compilation. *Paleoceanography*. https://doi.org/10.1029/2008PA001683

Day-Stirrat, R. J., Loucks, R. G., Milliken, K. L., Hillier, S., & van der Pluijm, B. A. (2008). Phyllosilicate orientation demonstrates early timing of compactional stabilization in calcite-cemented concretions in the Barnett Shale (Late Mississippian), Fort Worth Basin, Texas (U.S.A). *Sedimentary Geology, 208*, 27–35.

De Wall, H., & Warr, L. N. (2004). Oblique magnetic fabric in siderite-bearing pelitic rocks of the Upper Carboniferous Culm Basin, SW England: An indicator for palaeo-fluid migration? *Geological Society, London, Special Publications, 238*(1), 493–507.

Dhami, N. K., Greenwood, P. F., Poropat, S. F., Vijay, H., Brosnan, L., Holman, A. I., Campbell, M., Hopper, P., Smith, L., Jian, A., & Grice, K. (2023). Microbially mediated fossil concretions and their characterization by the latest methodologies: A review. *Frontiers in Microbiology, 14*, 1225411.

Ferré, E. C. (2002). Theoretical models of intermediate and inverse AMS fabrics. *Geophysical Research Letters, 29*(7), 1127. https://doi.org/10.1029/2001GL014367

Froelich, P., Klinkhammer, G. P., Bender, M. L., Luedtke, N. A., Heath, G. R., Cullen, D., Dauphin, P., Hammond, D., Hartman, B., & Maynard, V. (1979). Early oxidation of organic matter in pelagic sediments of the eastern equatorial Atlantic: suboxic diagenesis. *Geochimica et cosmochimica acta, 43*(7), 1075–1090.

García-Lasanta, C., Oliva-Urcia, B., Casas-Sainz, A. M., Román-Berdiel, T., Izquierdo-Llavall, E., Soto, R., Calvín, P., Mussaid, B., El Ouardi, H., Kullberg, J. C., & Villalaín, J. J. (2018). Inversion tectonics and magnetic fabrics in Mesozoic basins of the Western Tethys: A review. *Tectonophysics, 745*, 1–23.

Girdler, R. W. (1961). The measurement and computation of anisotropy of magnetic susceptibility in rocks. *Geochimica et Cosmochimica Acta, 5*, 34–44.

González-Lanchas, A., Remacha, E., Oms, O., Sierro, F. J., & Flores, J. A. (2019). Middle Eocene calcareous nannofossils in the Jaca transect (South-central Pyrenees Eocene Basin, Aragón river valley, Huesca). *Spanish journal of palaeontology*, *34*(2), 229–240.

Hoareau, G., Odonne, F., Debroas, E. J., Maillard, A., Monnin, C., & Callot, P. (2009). Dolomitic concretions in the Eocene Sobrarbe delta (Spanish Pyrenees): Fluid circulation above a submarine slide scar infilling. *Marine and Petroleum Geology, 26*(5), 724–737.

Hounslow, M. W. (2001). The crystallographic fabric and texture of siderite in concretions: Implications for siderite nucleation and growth processes. *Sedimentology, 48*(3), 533–557.

Ihmlé, P. F., Hirt, A. M., Lowrie, W., & Dietrich, D. (1989). Inverse magnetic fabric in deformed limestones of the Morcles nappe, Switzerland. *Geophysical Research Letters*, *16*(12), 1383–1386.

Izquierdo-Llavall, E., Sainz, A. C., Oliva-Urcia, B., Burmester, R., Pueyo, E. L., & Housen, B. (2015). Multi-episodic remagnetization related to deformation in the Pyrenean Internal Sierras. *Geophysical Journal International, 201*(2), 891–914.

Jackson, M., Gruber, W., Marvin, J., & Banerjee, S. K. (1988). Partial anhysteretic remanence and its anisotropy: Applications and grainsize-dependence. *Geophysical Research Letters, 15*(5), 440–443.

Jelinek, V. (1981). Characterization of the magnetic fabric of rocks. *Tectonophysics, 79*(3–4), T63–T67.

Labaume, P., Séguret, M., & Seyve, C. (1985). Evolution of a turbiditic foreland basin and analogy with an accretionary prism: Example of the Eocene south-Pyrenean basin. *Tectonics, 4*(7), 661–685.

Larrasoaña, J. C., Parés, J. M., & Pueyo, E. L. (2003). Stable Eocene magnetization carried by magnetite and iron sulphides in marine marls (Pamplona-Arguis formation, southern Pyrenees, northern Spain). *Studia Geophysica Et Geodaetica, 47*, 237–254.

Larrasoaña, J. C., Pueyo, E. L., & Parés, J. M. (2004). An integrated AMS, structural, palaeo-and rock-magnetic study of Eocene marine marls from the Jaca-Pamplona basin (Pyrenees, N Spain); new insights into the timing of magnetic fabric acquisition in weakly deformed mudrocks. *Geological Society, London, Special Publications, 238*(1), 127–143.

Läuchli, C., Garcés, M., Beamud, E., Valero, L., Honegger, L., Adatte, T., Spangenberg, J. E., Clark, J., Puigdefàbregas, C., Fildani, A., Kaenel, E., Hunger, T., Owak, A., & Castelltort, S. (2021). Magnetostratigraphy and stable isotope stratigraphy of the middle-Eocene succession of the Ainsa basin (Spain): New age constraints and implications for sediment delivery to the deep waters. *Marine and Petroleum Geology, 132*, 105182.

Lowrie, W. (1990). Identification of ferromagnetic minerals in a rock by coercivity and unblocking temperature properties. *Geophysical Research Letters, 17*(2), 159–162.

Mansurbeg, H., Caja, M. A., Marfil, R., Morad, S., Remacha, E., Garcia, D., Martín-Crespo, T., El-Ghali, M. A. K., & Nystuen, J. P. (2009). Diagenetic evolution and porosity destruction of turbiditic hybrid arenites and siliciclastic sandstones of foreland basins: Evidence from the Eocene Hecho Group, Pyrenees, Spain. *Journal of Sedimentary Research, 79*(9), 711–735.

McCabe, C., Jackson, M., & Ellwood, B. B. (1985). Magnetic anisotropy in the Trenton limestone: Results of a new technique, anisotropy of anhysteretic susceptibility. *Geophysical Research Letters, 12*(6), 333–336.

Muñoz, J. A. (1992). Evolution of a continental collision belt: ECORS-Pyrenees crustal balanced cross-section. *Thrust tectonics* (pp. 235–246). Springer.

Mutti, E. (1977). Distinctive thin-bedded turbidite facies and related depositional environments in the Eocene Hecho Group (South-Central Pyrenees, Spain). *Sedimentology, 24*(1977), 107–131.

Mutti, E., Tinterri, R., Remacha, E., Mavilla, N., Angella, S., & Fava, L. (1999). *AAPG continuing education course note series# 39: An introduction to the analysis of ancient turbidite basins from an outcrop perspective*. American Association of Petroleum Geologists.

Oliva-Urcia, B., Casas, A. M., Pueyo, E. L., & Pocoví, A. (2012). Structural and paleomagnetic evidence for non-rotational kinematics in the western termination of the External Sierras (southwestern central Pyrenees). *Geologica Acta, 10*(2), 125–144.

Oliva-Urcia, B., Larrasoaña, J. C., Pueyo, E. L., Gil, A., Mata, P., Parés, J. M., Schleicher, A. M., & Pueyo, O. (2009). Disentangling magnetic subfabrics and their link to deformation processes in cleaved sedimentary rocks from the Internal Sierras (west central Pyrenees, Spain). *Journal of Structural Geology, 31*(2), 163–176.

Oms, O., Dinarès-Turell, J., & Remacha, E. (2003). Magnetic stratigraphy from deep clastic turbidites: an example from the Eocene Hecho group (southern Pyrenees). *Studia Geophysica et Geodaetica*, *47*, 275–288.

Parés, J. M., & van der Pluijm, B. A. (2002). Phyllosilicate fabric characterization by low-temperature anisotropy of magnetic susceptibility (LT-AMS). *Geophysical Research Letters, 29*(24), 68–71.

Payros, A., Pujalte, V., & Orue-Etxebarria, X. (1999). The South Pyrenean Eocene carbonate megabreccias revisited: New interpretation based on evidence from the Pamplona Basin. *Sedimentary Geology, 125*(3–4), 165–194.

Peris-Cabré, S., Valero, L., Spangenberg, J. E., Vinyoles, A., Verité, J., Adatte, T., Tremblin, N., Watkins, S., Sharma, N., Garcés, M., Puigdefàbregas, C., & Castelltort, S. (2023). Fluvio-deltaic record of increased sediment transport during the Middle Eocene Climatic Optimum (MECO), Southern Pyrenees, Spain. *Climate of the past, 19*(3), 533–554.

Petrash, D. A., Bialik, O. M., Bontognali, T. R., Vasconcelos, C., Roberts, J. A., McKenzie, J. A., & Konhauser, K. O. (2017). Microbially catalyzed dolomite formation: From near-surface to burial. *Earth-Science Reviews, 171*, 558–582.

Pueyo Anchuela, Ó., Gil Imaz, A., & Pocoví Juan, A. (2010). Significance of AMS in multilayer systems in fold-and-thrust belts. A case study from the Eocene turbidites in the Southern Pyrenees (Spain). *Geological Journal, 45*(5–6), 544–561. https://doi.org/10.1002/gj.1194

Pueyo-Anchuela, O., Casas-Sainz, A. M., Pocoví-Juan, A., & Gil-Imaz, A. (2011). Lithology-dependent reliability of AMS analysis: A case study of the Eocene turbidities in the southern Pyrenees (Aragón, Spain). *Comptes Rendus Geoscience, 343*(1), 11–19.

Puigdefàbregas, C. (1975). La sedimentación molásica en la cuenca de Jaca. Pirineos, 104, 1–188. http://hdl.handle.net/10261/82989

Pujalte, V., Schmitz, B., Caballero, J. B., Orue-Echebarría, X., Bilbao, G. B., Dinarès-Turell, J., & Santamaria, F. C. (2009). Correlation of the Thanetian-Ilerdian turnover of larger foraminifera and the Paleocene-Eocene thermal maximum: confirming evidence from the Campo area (Pyrenees, Spain). *Geologica Acta*. https://doi.org/10.1344/105.000000276

Raiswell, R., & Fisher, Q. J. (2004). Rates of carbonate cementation associated with sulphate reduction in DSDP/ODP sediments: Implications for the formation of concretions. *Chemical Geology, 211*(1–2), 71–85.

Reinhold, C. (1998). Multiple episodes of dolomitization and dolomite recrystallization during shallow burial in Upper Jurassic shelf carbonates: Eastern Swabian Alb, southern Germany. *Sedimentary Geology, 121*(1–2), 71–95.

Remacha, E., Fernandez, L. P., & Maestro, E. (2005). The transition between sheet-like lobe and basin-plain turbidites in the Hecho Basin (South-Central Pyrenees, Spain). *Journal of Sedimentary Research, 75*(5), 798–819.

Roberts, A. P. (2015). Magnetic mineral diagenesis. *Earth-Science Reviews, 151*, 1–47.

Roberts, A. P., & Weaver, R. (2005). Multiple mechanisms of remagnetization involving sedimentary greigite (Fe3S4). *Earth and Planetary Science Letters, 231*(3–4), 263–277.

Rochette, P. (1988). Inverse magnetic fabric in carbonate-bearing rocks. *Earth and Planetary Science Letters, 90*(2), 229–237.

Rochette, P., Jackson M., & Aubourg C. (1992). Rock magnetism and the interpretation of anisotropy of magnetic susceptibility. *Reviews of Geophysics*, *30*(3), 209–226.

Ruiz, M., Gaspà, O., Gallart, J., Díaz, J., Pulgar, J. A., García-Sansegundo, J., & González-Cortina, J. M. (2006). Aftershocks series monitoring of the September 18, 2004 M = 4.6 earthquake at the western Pyrenees: A case of reservoir-triggered seismicity? *Tectonophysics, 424*(3–4), 223–243.

Schmitz, B., & Pujalte, V. (2003). Sea-level, humidity, and land-erosion records across the initial Eocene thermal maximum from a continental-marine transect in northern Spain. *Geology, 31*(8), 689–692.

Schmitz, B., Pujalte, V., & Nunez-Betelu, K. (2001). Climate and sea-level perturbations during the Incipient Eocene Thermal Maximum: Evidence from siliciclastic units in the Basque Basin (Ermua, Zumaia and Trabakua Pass), northern Spain. *Palaeogeography, Palaeoclimatology, Palaeoecology, 165*(3–4), 299–320.

Sellés-Martínez, J. (1996). Concretion morphology, classification and genesis. *Earth-Science Reviews, 41*(3–4), 177–210.

Stakes, D. S., Orange, D., Paduan, J. B., Salamy, K. A., & Maher, N. (1999). Cold-seeps and authigenic carbonate formation in Monterey Bay, California. *Marine Geology, 159*, 93–109.

Tarling, D., & Hrouda, F. (Eds.). (1993). *Magnetic anisotropy of rocks*. Springer Science & Business Media.

Teixell, A. (1996). The Ansó transect of the southern Pyrenees: Basement and cover thrust geometries. *Journal of the Geological Society, 153*(2), 301–310.

Teixell, A. (1998). Crustal structure and orogenic material budget in the west central Pyrenees. *Tectonics, 17*(3), 395–406.

Torres, M. E., Hong, W. L., Solomon, E. A., Milliken, K., Kim, J. H., Sample, J. C., Teichert, B. M. A., & Wallmann, K. (2020). Silicate weathering in anoxic marine sediment as a requirement for authigenic carbonate burial. *Earth-Science Reviews, 200*, 102960.

Travé, A., Labaume, P., Calvet, F., & Soler, A. (1997). Sediment dewatering and pore fluid migration along thrust faults in a foreland basin inferred from isotopic and elemental geochemical analyses (Eocene southern Pyrenees, Spain). *Tectonophysics, 282*(1–4), 375–398.

Vinyoles, A., López-Blanco, M., Garcés, M., Arbués, P., Valero, L., Beamud, E., Oliva-Urcia, B., & Cabello, P. (2021). 10 Myr evolution of sedimentation rates in a deep marine to non–marine

foreland basin system: Tectonic and sedimentary controls (Eocene, Tremp–Jaca Basin, Southern Pyrenees, NE Spain). *Basin Research*, *33*(1), 447–477.

Wanas, H. A. (2008). Calcite-cemented concretions in shallow marine and fluvial sandstones of the Birket Qarun Formation (Late Eocene), El-Faiyum depression, Egypt: Field, petrographic and geochemical studies: Implications for formation conditions. *Sedimentary Geology, 212*(1–4), 40–48.